

# Lunar Low-Titanium Magmatism during Ancient Expansion inferred from Ejecta originating from Linear Gravity Anomalies

Gaku Nishiyama<sup>1</sup>, Tomokatsu Morota<sup>2</sup>, Noriyuki Namiki<sup>3</sup>, Kazuki Inoue<sup>2</sup>, and Seiji Sugita<sup>1</sup>

<sup>1</sup>University of Tokyo

<sup>2</sup>The University of Tokyo

<sup>3</sup>National Astronomical Observatory

August 4, 2023

## Abstract

Linear gravity anomalies (LGAs) on the Moon have been interpreted as ancient magmatic intrusions formed during the lunar expansion. The composition of such ancient subsurface intrusions may offer a hint for the lunar thermodynamic state in the initial stage of lunar history. To pose a first compositional constraint on magmatism related to lunar expansion, this study analyzed the spectrum and gravity around craters on LGAs, such as Rowland, Roche, and Edison craters. Using spectral datasets around the craters, we first surveyed non-mare basaltic exposures that we hypothesize originate from subsurface intrusions. This hypothesis is then investigated in comparison between the GRAIL data and post-cratering gravity simulated with the iSALE shock physics code. Our spectral analysis reveals no basaltic exposure around Rowland crater. Further, the observed termination of LGA at the crater rim contradicts the gravity simulation which assumes that LGA predates Rowland crater. These results suggest that LGA formation postdates the Rowland formation and that lunar expansion lasted even after the Nectarian age. On the other hand, we found that both Roche and Edison craters possess basaltic exposures in their peripheries. Because the gravity reduced inside Roche crater can be reproduced in our simulation, the discovered basaltic exposures are possibly LGA materials ejected from these craters. The composition of those exposures suggests that the LGA intrusions are composed of low-titanium magma. This indicates that ancient magma during the expansion did not contain ilmenite-rich melt provided by a plume ascending from the ilmenite-bearing layer above the core.

## Hosted file

970204\_0\_art\_file\_11239237\_rykbkr.docx available at <https://authorea.com/users/645023/articles/657662-lunar-low-titanium-magmatism-during-ancient-expansion-inferred-from-ejecta-originating-from-linear-gravity-anomalies>

## Hosted file

970204\_0\_supp\_11239203\_rykpf5.docx available at <https://authorea.com/users/645023/articles/657662-lunar-low-titanium-magmatism-during-ancient-expansion-inferred-from-ejecta-originating-from-linear-gravity-anomalies>

1  
2 **Lunar Low-Titanium Magmatism during Ancient Expansion inferred from Ejecta**  
3 **originating from Linear Gravity Anomalies**  
4

5 **G. Nishiyama<sup>1,2</sup>, T. Morota<sup>1</sup>, N. Namiki<sup>1,2,3</sup>, K. Inoue<sup>1</sup>, S. Sugita<sup>1</sup>**

6 <sup>1</sup> The Department of Earth and Planetary Science, The University of Tokyo, Tokyo, Japan.

7 <sup>2</sup> National Astronomical Observatory of Japan, Mitaka, Japan.

8 <sup>3</sup> The Graduate University for Advanced Studies, SOKENDAI, Hayama, Japan.

9  
10 Corresponding author: Gaku Nishiyama (gaku.nishiyama@grad.nao.ac.jp)

11 **Key Points:**

- 12
- 13 • Magma composition during lunar ancient expansion is investigated with spectrum and gravity around craters on linear gravity anomalies.
  - 14 • High-calcium pyroxene exposures and gravity reduction around Roche crater imply an excavation of subsurface ancient dikes.
  - 15 • Subsurface dikes formed during the expansion stage are estimated to be composed of
  - 16 low-titanium magma.
  - 17
  - 18

## 19 **Abstract**

20 Linear gravity anomalies (LGAs) on the Moon have been interpreted as ancient magmatic  
21 intrusions formed during the lunar expansion. The composition of such ancient subsurface  
22 intrusions may offer a hint for the lunar thermodynamic state in the initial stage of lunar history.  
23 To pose a first compositional constraint on magmatism related to lunar expansion, this study  
24 analyzed the spectrum and gravity around craters on LGAs, such as Rowland, Roche, and Edison  
25 craters. Using spectral datasets around the craters, we first surveyed non-mare basaltic exposures  
26 that we hypothesize originate from subsurface intrusions. This hypothesis is then investigated in  
27 comparison between the GRAIL data and post-cratering gravity simulated with the iSALE shock  
28 physics code. Our spectral analysis reveals no basaltic exposure around Rowland crater. Further,  
29 the observed termination of LGA at the crater rim contradicts the gravity simulation which  
30 assumes that LGA predates Rowland crater. These results suggest that LGA formation postdates  
31 the Rowland formation and that lunar expansion lasted even after the Nectarian age. On the other  
32 hand, we found that both Roche and Edison craters possess basaltic exposures in their  
33 peripheries. Because the gravity reduced inside Roche crater can be reproduced in our  
34 simulation, the discovered basaltic exposures are possibly LGA materials ejected from these  
35 craters. The composition of those exposures suggests that the LGA intrusions are composed of  
36 low-titanium magma. This indicates that ancient magma during the expansion did not contain  
37 ilmenite-rich melt provided by a plume ascending from the ilmenite-bearing layer above the  
38 core.

39

## 40 **Plain Language Summary**

41 The Moon has positive, narrow, and long gravity anomalies, so-called linear gravity  
42 anomalies (LGAs), which are believed to be ancient magmatic intrusions formed during the lunar  
43 ancient expansion. The composition of these intrusions could provide insights into the early lunar  
44 thermal state. In this study, we analyzed the spectra and gravity data around craters located on  
45 LGAs, specifically Rowland, Roche, and Edison craters, which might have ejected the LGA  
46 material. By analyzing the spectral data, we first identified non-mare basaltic exposures that  
47 likely originate from these subsurface formations. We next examine if these exposures are  
48 composed of the LGA materials, by comparing the observed data with a simulation of gravity  
49 after cratering events. We found no basaltic exposures around Rowland and that gravity inside  
50 Rowland is not consistent with the excavation hypothesis, suggesting that LGA formation and  
51 lunar expansion occurred after the Rowland formation. On the other hand, we discovered basaltic  
52 exposures around both Roche and Edison craters. The gravity inside Roche crater manifests that  
53 the discovered basaltic exposures were ejected from the LGAs. The composition of these  
54 exposures indicates that LGAs are composed of low-titanium magma, which provides a new  
55 constraint on the ancient thermal state of the Moon.

## 56 **1 Introduction**

57 The early expansion stage of the Moon following its formation is a key to understanding  
58 the thermal evolution of the lunar interior. Many lunar evolutionary models have suggested that  
59 the Moon might have an expansion state in its thermal history (Laneuville et al., 2013; U et al.,  
60 2022; N. Zhang et al., 2013a, 2013b). Petrological studies have indicated that the Moon had a  
61 layer of ilmenite-bearing cumulates (IBC) between its anorthositic crust and olivine-

62 orthopyroxene mantle immediately after solidifying the lunar magma ocean (Elkins-Tanton et  
63 al., 2011; Snyder et al., 1992). It has been hypothesized that this dense layer drove a gravitational  
64 instability and consequently a mantle overturn, releasing gravitational potential into heat. The  
65 overturn could simultaneously transport heat-producing elements to the lunar core-mantle  
66 boundary zone, producing radiogenic heat in the deep area of the Moon (e.g., Hess & Parmentier,  
67 1995). The following rise of the lunar temperature may have caused thermal expansion of the  
68 lunar volume in the early stage of the Moon (Laneuville et al., 2013; Zhang et al., 2013a, 2013b).  
69 This process coincides with melt generation and migration, which could also play a crucial role  
70 in the lunar volumetric change (U et al., 2022). The duration of lunar radius change depends on  
71 the initial thermal state and lunar inner structures. Thus, temporal constraints on ancient lunar  
72 expansion are essential hints to elucidate thermal history.

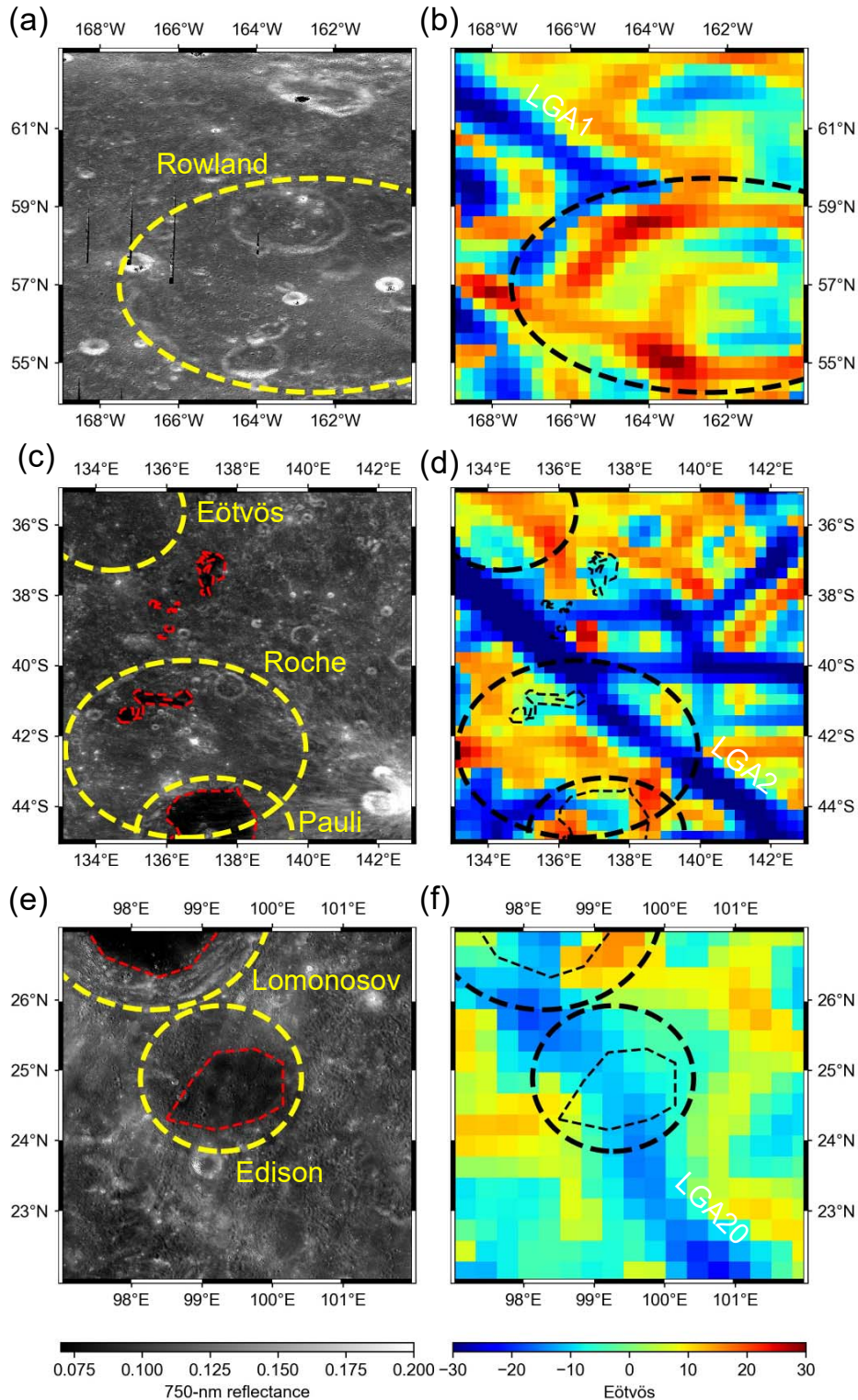
73 Together with such chronological information, the composition of the produced magma  
74 accompanied by the lunar expansion is essential to understand the source property and related  
75 evolutionary processes inside the Moon. The lunar surface holds maria of volcanic basalt, whose  
76 age peaks at 3.2–3.8 Ga and another peak around 2.0 Ga in the Procellarum KREEP Terrain  
77 (PKT) region (e.g., Hiesinger et al., 2003; Morota et al., 2011). The composition of lunar maria  
78 is known to vary with time. For example, the titanium content of the PKT maria increases by a  
79 few percent around 2.3 Ga (Kato et al., 2017; Sato et al., 2017). This transition indicates a  
80 change of magma source composition, possibly related to a hot plume containing IBC material.  
81 In addition to the present-exposed mare, several works have identified ancient basalt covered  
82 with highland regolith, the so-called cryptomare (e.g., Giguere et al., 2003; Whitten & Head,  
83 2015a,b). Spectral comparison between cryptomare and lunar regolith samples has shown that  
84 low-titanium basalt matches ancient cryptomare basalts the most closely (Whitten & Head,  
85 2015b). These combinations of temporal and compositional information on magmatism are  
86 essential to elucidate the lunar thermal history. However, no compositional constraints on  
87 magmatism directly related to the ancient expansion have been posed because magmatism during  
88 the global expansion is invisible in the surficial data solely.

89 In order to survey the geologic information related to the expansion, regions above lunar  
90 linear gravity anomalies (LGAs) are of particular interest. The NASA Gravity Recovery and  
91 Interior Laboratory (GRAIL) mission obtained high-resolution lunar gravity data (Zuber et al.,  
92 2013), enabling the identification of linear positive Bouguer anomalies with lengths of over-  
93 hundred kilometers (Andrews-Hanna et al., 2013). Based on their narrow and long geometries,  
94 LGAs have been interpreted as ancient vertical tabular intrusions or dikes denser than the  
95 surrounding crust. The random orientations of LGAs on both near- and farsides suggest that  
96 LGAs were formed under a globally-isotropic extension of the lithosphere (Andrews-Hanna et  
97 al., 2013). Furthermore, Sawada et al. (2016) have revealed that LGAs overlap topographic  
98 depressions like terrestrial great rift valleys, similarly indicating horizontal tensile stress during  
99 the LGA formation.

100 We emphasize that highland areas covering LGAs and superposing craters are the best  
101 locations to find evidence of ancient magmatism. Some LGAs are superposed by large craters,  
102 such as Rowland crater on LGA1 (Figure 1a and b), Roche crater on LGA2 (Figure 1c and d),  
103 Crisium basin on LGA4, and Edison crater on LGA20 (Figure 1e and f). Note that the LGA are  
104 numbered in the same way as Andrews-Hanna et al. (2013) and Sawada et al. (2016). Based on  
105 the previous estimation of LGA structures, the top depth of intrusions could be about 10 km in  
106 the shallowest case (Liang & Andrews-Hanna, 2022). Thus, these craters possibly excavated a

107 certain fraction of LGA materials. LGA material originally from a partially molten region in the  
108 mantle contains high-calcium pyroxenes (HCP) like lunar maria. This makes it impossible to  
109 identify excavated intrusions spectrally around Crisium basin, which is covered with mare  
110 basalts. On the other hand, spectra of highland regions are dominated by low-calcium pyroxenes  
111 (LCP), which have absorption features different from HCP (Cloutis & Gaffey, 1991; Denevi et  
112 al., 2007; Klima et al., 2007, 2011; Lucey et al., 2014; Ogawa et al., 2011; Yamamoto et al.,  
113 2015). Therefore, if highland craters (Rowland, Roche, and Edison) excavated LGA materials,  
114 distinguishable spectra of exposures might be found in the peripheries of those craters.  
115 Incorporating the chronological information of the craters and the cross-cutting relationships  
116 between these LGAs and craters, the age of the LGA formation could also be constrained by the  
117 presence of excavated materials.

118 To investigate the composition of ancient magmatism and the chronology of the initial  
119 lunar expansion, this paper analyzes the geology around Rowland, Roche, and Edison craters in  
120 terms of the LGA material and history. We first show the spectral features in the continuous  
121 ejecta region of these craters by finding candidates of basaltic exposures in a multiband  
122 reflectance map to see if they contain mare-like HCP and estimate the FeO and TiO<sub>2</sub> contents.  
123 Then, we investigate whether these exposures originated from the LGA material. Later in this  
124 paper, we simulate deformation and excavation during the cratering process to confirm the  
125 possibility of excavation in comparison with gravity data around LGA. Finally, we propose  
126 compositional properties of ancient magma sources and discuss the ancient lunar magmatic and  
127 thermal evolution.



128  
129  
130  
131  
132

**Figure 1.** The Kaguya/MI 750-nm reflectance (a, c, e) and GRAIL gravity gradient maps (b, d, f) of regions analyzed in this paper. Crater rims are shown in the yellow and black lines on the reflectance and gravity gradient maps, respectively. Small maria are shown as the red and black lines on the reflectance and gravity gradient maps, respectively. The LGAs are traced with white

133 dashed lines on the gravity gradient maps. (a, b) Rowland crater and LGA1. LGA1 seems to  
134 terminate around the rim of Rowland crater. (c, d) Roche crater and LGA2. LGA2 penetrates  
135 throughout Roche crater. This region possesses small maria (Pasckert et al., 2015a). (e, f) Edison  
136 crater and LGA20. LGA20 seems to cross Edison crater.

137

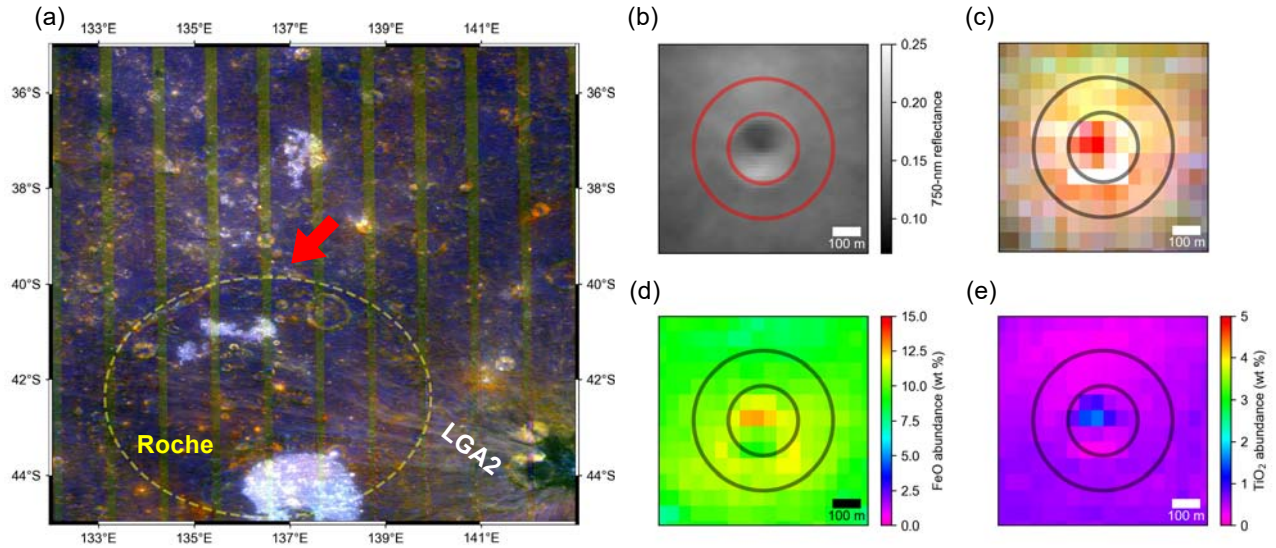
## 138 2 Spectral analysis method

139 To identify probable ancient magma exposures, we analyzed spectral datasets obtained by  
140 previous lunar missions, following two steps. First, we made a compositional map within the  
141 targeted area by using the Multiband Imager (MI) data (Ohtake et al., 2008) taken by the  
142 Japanese lunar orbiter Kaguya. MI has the advantage of mapping the material distribution with a  
143 high spatial resolution, but it is still difficult to distinguish between LCP and HCP from MI  
144 whose spectral resolution is not sufficient to determine 1000- and 2000-nm absorption centers of  
145 pyroxenes. Therefore, we complementally analyzed hyperspectral data from the Moon  
146 Mineralogy Mapper (M<sup>3</sup>) onboard the Chandrayaan-1 spacecraft.

### 147 2.1 MI map data analysis

148 Our analysis used MI\_MAP products that include mosaics of reflectance at nine bands  
149 from visible to near-infrared wavelengths. The MI camera is equipped with five visible (415,  
150 750, 900, 950, and 1000 nm) and four near-infrared (1000, 1050, 1250, and 1550 nm) bands. The  
151 published MI\_MAP products have already been normalized by a photometric function with local  
152 topography, corrected via a reflectance comparison between the Apollo-16 sampling site and a  
153 lunar soil sample (Ohtake et al., 2008, 2013; Yokota et al., 2011). The spatial resolution of  
154 MI\_MAP is 2048 pixels/degree, corresponding to 15 m at the equator. However, accuracy of  
155 image registration is not so high that we binned the data by 4×4 pixels to reduce the error. Also,  
156 some values are unreasonably lower than zero because of shadows in steep areas such as crater  
157 walls. Thus, we neglected such pixels for this binning process and in the latter analysis.

158 Searching for fresh basaltic materials, we made an RGB color composite map of spectral  
159 absorption depths (M. Ohtake et al., 2014; Taguchi et al., 2017) (**Figure 2a**). First, we  
160 normalized the spectrum by a continuum between 750 and 1550 nm at each binned pixel and  
161 mapped the absorption depths from the continuum at 950, 1050, and 1250 nm. Then, we  
162 composited these three maps as RGB (red: 950 nm; green: 1050 nm; blue: 1250 nm). Olivine and  
163 pyroxene that comprise lunar basalts exhibit spectral depressions at these bands, so basaltic  
164 materials are shown in whiter colors. On the contrary, anorthosite exposure appears blue due to a  
165 lack of absorption at the 950- and 1050-nm bands. In addition, space weathering on the Moon  
166 generally weakens the absorption features of minerals, so fresh materials are brighter on the map.



167

168 **Figure 2.** (a) RGB composite map around LGA2. (b-e) Maps of 750-nm reflectance, RGB  
 169 composite, FeO abundance, and TiO<sub>2</sub> abundance at P1 (indicated by the red arrow in (a)). The  
 170 red or black lines show circles with one and two radii of the fresh crater whose inside is filled  
 171 with basaltic material. Note that the images except for (b) are binned by 4×4 pixels.

172 We next selected candidates of basaltic exposures from the composite map by visual  
 173 inspections and categorized them morphologically (**Figure 2b**). Comparing topography from  
 174 SLDEM2015 (Barker et al., 2016) with 750-nm reflectance maps, we carefully chose spots  
 175 whose colors are white on the map (**Figure 2c**). The fresh material is generally exposed around  
 176 new craters or at steep slopes, so we attached flags, such as “crater” or “slope”, to the selected  
 177 places, depending on their morphologies. It should be noted that white spots in topographically  
 178 low areas are excluded because these sites are perhaps small maria. As endmember spectra for  
 179 the latter analysis, we also extracted data in both highland and mare that particularly exhibit high  
 180 Optical Maturity Parameter (OMAT) values and, therefore, are fresh (Lucey et al., 2000).

181 Finally, we characterized compositions around the candidates. From empirical algorithms  
 182 deriving iron and titanium contents from MI reflectance ratios (Lucey et al., 2000; Otake et al.,  
 183 2012), FeO and TiO<sub>2</sub> distribution were calculated. We then estimated their average and standard  
 184 deviation for each location. At exposures on slopes, we manually fitted a circle on white pixels  
 185 and simply averaged values. In the case of craters, we averaged values outside a circle fitted to  
 186 the crater rim, as shown in **Figure 2d** and **e**. Depending on the illumination conditions,  
 187 reflectance values occasionally become unrealistic within craters, making iron and titanium  
 188 contents too high or low. To avoid significant errors due to these problems, we calculate the  
 189 azimuthal average and standard deviation of area 1–2 crater radii away from its center. This  
 190 region is covered by continuous ejecta (Melosh, 1989; Moore et al., 1974), allowing us to treat it  
 191 as a representative value of materials exposed by the fresh crater.

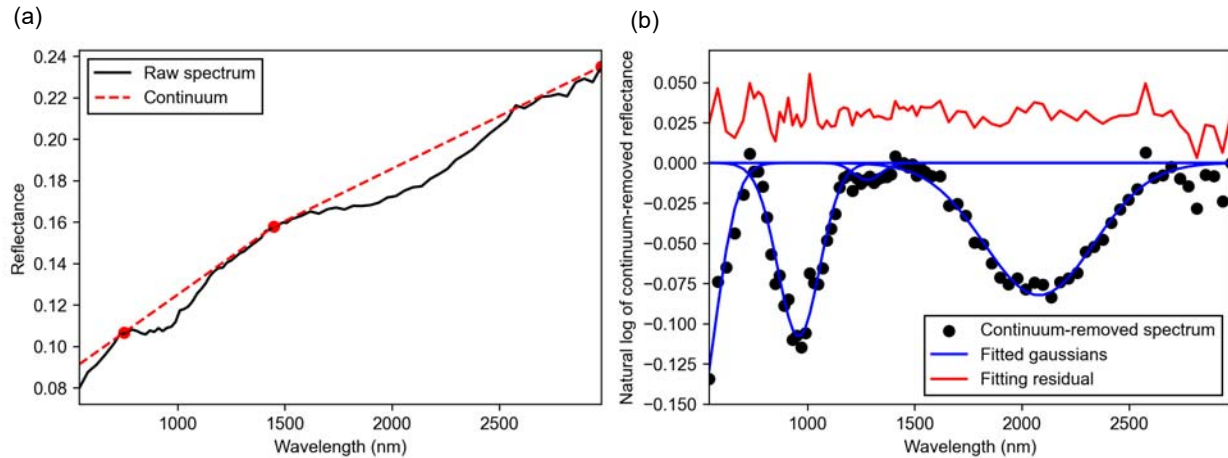
## 192 2.2 M<sup>3</sup> data analysis

193 We analyzed hyperspectral reflectance around the candidates using the M<sup>3</sup> L2 products.  
 194 M<sup>3</sup> was an imaging spectrometer that obtained cube images composed of two spatial and one

195 spectral dimensions. M<sup>3</sup> covered wavelengths approximately from 400 to 3000 nm with spatial  
196 resolutions of 70–140 and 140–280 m/pixel for Target and Global modes, depending on the  
197 spacecraft altitude (Green et al., 2011; Pieters et al., 2009). The reflectance data have been  
198 published as the L2 products after solar irradiance correction, statistical polishing, removal of  
199 thermal emission, and photometric correction (Besse et al., 2013; Boardman et al., 2011; Clark et  
200 al., 2011; Green et al., 2011; Isaacson et al., 2013). It should be noted that the ground truth  
201 correction is not applied to the L2 product, but the correction factor derived from the average  
202 62231 soil is also published in the M<sup>3</sup> data archive. It is well known that this correction improves  
203 the characterization of the 1000-nm absorption position on highland soil. The correction factor  
204 varies depending on M<sup>3</sup> optical periods because a wide range of the detector temperature due to  
205 the solar zenith angle generates artifacts in the acquired spectra (Isaacson et al., 2013).  
206 Therefore, we applied the correction factors of corresponding optical periods to each L2 product  
207 in the latter analysis.

208 As a preprocess prior to the determination of pyroxene type at each location, a continuum  
209 was subtracted from the corrected reflectance in the same manner as Whitten & Head (2015b).  
210 Due to space weathering, lunar spectra have a red-sloped continuum, which disturbs the analysis  
211 of accurate mineralogical absorption and has been removed in previous lunar hyperspectral  
212 characterization (e.g., Isaacson et al., 2011; Sunshine et al., 1990; Yamamoto et al., 2018;  
213 Yamamoto & Watanabe, 2021). For this continuum removal, our analysis employed the convex  
214 hull method that finds a polygonal line connecting three tie points (Figure 3a). The first tie point  
215 was set at 750 nm, but the second and third were able to vary in the wavelength range of 1329–  
216 1778 nm and over 2776 nm, respectively. The second and third tie points were selected so that  
217 the polygonal line among the three tie points did not intersect with the M<sup>3</sup> spectrum. Finally, the  
218 spectrum was divided by this two-parted linear continuum, and the band depth at each  
219 wavelength was calculated.

220 To identify the pyroxene type, the modified Gaussian model (MGM) was then applied to  
221 the continuum-removed spectra. MGM has been known as a robust algorithm to characterize  
222 pyroxene spectra in visible to near-infrared wavelengths (e.g., Denevi et al., 2007; Sunshine et  
223 al., 1990), in which the spectra can be deconvoluted to several Gaussians. The central  
224 wavelengths of deconvoluted Gaussians are significant indicators of pyroxene compositions.  
225 Based on previous reflectance analysis on natural and synthetic pyroxenes (Denevi et al., 2007;  
226 Klima et al., 2007, 2011), Gaussians centered at 900–1000 and 1800–2400 nm have their peaks  
227 at shorter wavelengths for LCP and vice versa for HCP. Additionally, HCP has an absorption at  
228 1300 nm, although LCP exhibits no absorption there. Therefore, our analysis fitted four  
229 Gaussians to the spectra by setting the initial centers of Gaussians at 300, 1000, 1300, and 2000  
230 nm in the same manner as Ogawa et al. (2011). The calculated band positions were finally  
231 compared with those of synthetic and natural LCP and HCP (Denevi et al., 2007; Klima et al.,  
232 2007, 2011). In order to avoid noisy spectral data in the latter discussion, exposures only with a  
233 maximum absorption depth at 900–1000 nm larger than 10 % and root-mean-square of fitting  
234 residual less than 0.02 are chosen. This limitation on the signal-to-noise ratio in our M<sup>3</sup> analysis,  
235 therefore, reduced the number of analyzed exposures from that in the MI data analysis.



236

237 **Figure 3.** Example of spectral analysis routine for  $M^3$  dataset. (a) One of the spectra at LGA2-E1  
 238 from the image of M3G20090529T060422. The spectrum after all the calibration is shown in  
 239 black. The red points correspond to tie points used for a two-parted linear continuum generation  
 240 shown as the red dashed line. (b) Demonstration of our MGM deconvolution. The black dots are  
 241 the natural log of reflectance values normalized by the continuum. The blue lines are four  
 242 Gaussians fitted to the continuum-removed reflectance. The fitting residual is shown in red with  
 243 an offset of 0.03.

### 244 3 Spectral features around LGAs

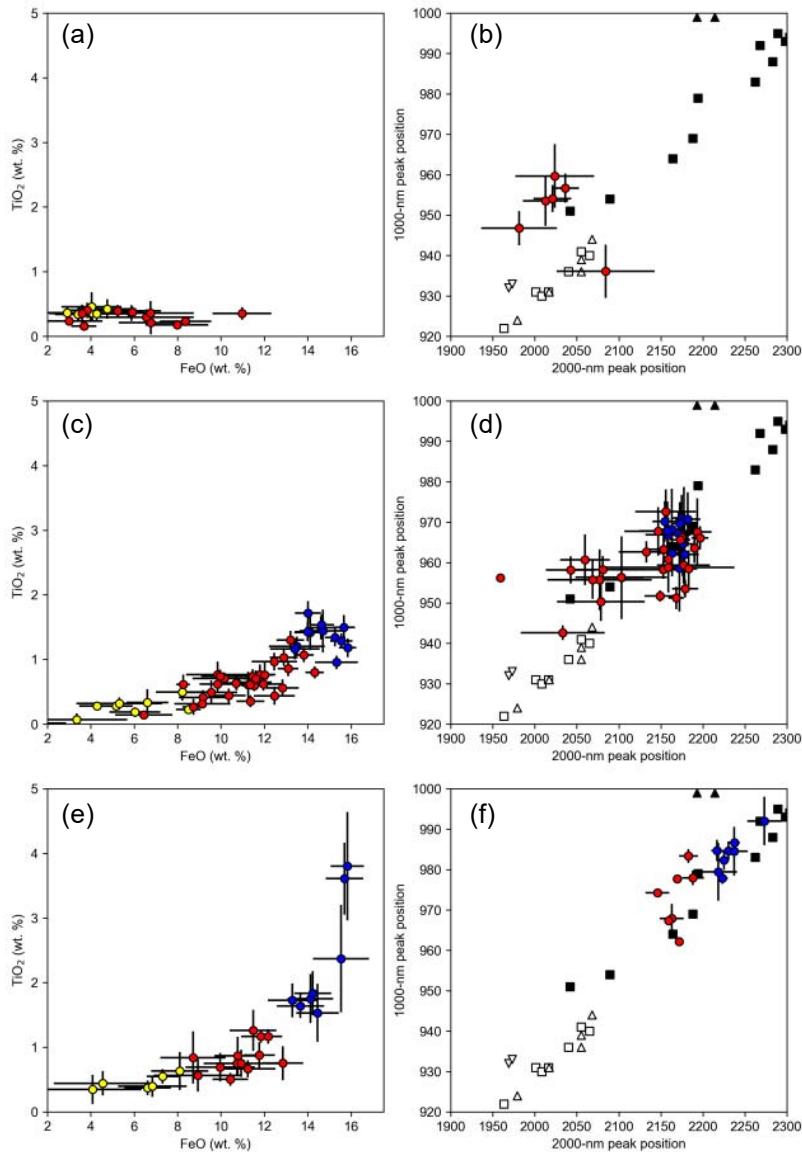
#### 245 3.1 LGA1

246 Around Rowland crater, the number of locations with white colors is much less than  
 247 LGA2 (Figure S1). We totally selected 13 pyroxene-rich exposure candidates inside and outside  
 248 Rowland crater and labeled them with a mark of exposure (E) and ID number. Note that the spots  
 249 inside Rowland were included in the analysis, too, because magmatic material could be mixed  
 250 within the crater during its formation. For comparison, we also extracted 8 anorthositic spots on  
 251 the composite map as typical highland materials. It should be noted that no maria exists in this  
 252 region (Figure 1a). The longitude and latitude of each location are summarized in Table S1.

253 The MI data around LGA1 revealed almost no signs of significantly high FeO and  $TiO_2$   
 254 abundances. The MI data of this region commonly exhibits FeO and  $TiO_2$  abundances lower than  
 255 4 wt.% and 1 wt.%, respectively (Figure S3 and S4). FeO and  $TiO_2$  abundances at the exposures  
 256 show the same tendency as other areas in Figure 4a. Except for a few candidates, such as E3,  
 257 FeO abundance in these exposures is less than half of that in typical maria (Figure 4c and e).  
 258 These values are within the range of noritic materials (Lucey et al., 1998), which is thought to be  
 259 a typical rock type of the lunar lower crust.

260 The  $M^3$  spectral features indicate that the pyroxene characteristic in this region is similar  
 261 to LCP. Figure 4b shows a comparison of the absorption peak positions at 1000- and 2000-nm  
 262 bands to laboratory LCP data. Owing to the low signal-to-noise ratio and weak absorption in the  
 263  $M^3$  data of this region, the number of candidates was limited. However, the calculated 2000-nm  
 264 peak positions were always shorter than 2100 nm, ranging similarly to the synthetic LCP data.  
 265 LCP is known to be dominant on the spectra of noritic rocks. Therefore, these pyroxene

266 exposures around LGA1 can be interpreted as materials ejected from the noritic lower crust, not  
 267 from basaltic magma intrusions composed of HCP.



268

269 **Figure 4.** Compositional summary of the spectral analysis results. FeO and TiO<sub>2</sub> abundance at  
 270 exposure candidates. The blue and red points correspond to pyroxene exposures on the highland  
 271 and maria labeled with E and M, respectively. The yellow points are highland crust exposures  
 272 with bluer colors on the composite map. (a, c, e) FeO and TiO<sub>2</sub> abundance at each location. The  
 273 error bar is a standard deviation of the value within the extracted area. (b, d, f) 1000- and 2000-  
 274 nm absorption peak positions at exposure candidates. The error bar is a standard deviation of the  
 275 M<sup>3</sup> pixels of those candidates. The black square and triangles are synthetic clinopyroxene (HCP)  
 276 data from Denevi et al. (2007) and Klima et al. (2011), respectively. The white squares and  
 277 triangles are synthetic and natural orthopyroxene (LCP) data from Denevi et al. (2007) and  
 278 Klima et al. (2007), respectively. Results are summarized for each region: (a, b) around LGA1,  
 279 (c, d) around LGA2, and (e, f) around LGA20.

280

## 281 3.2 LGA2

282 From the MI composite map around LGA2, we found 31 white exposures in the northern  
283 area of Roche crater. Because Roche crater is superposed by Pauli crater, the southern part of this  
284 area is excluded conservatively in this study (Figure 1). The eastern side of Roche is not  
285 analyzed, either, due to contamination by bright ejecta rays from the Eratosthenian-aged Ryder  
286 crater.

287 It is noteworthy that this region contains small maria between Eötvös and Roche craters  
288 (Figure 1). Pasckert et al. (2015) and Wilhelms & El-Baz (1977) have already identified young  
289 mare patches inside Roche and Pauli craters. Our comparison between the composite and  
290 topography map reveals four additional candidates of mare patches in the northern part of Roche  
291 (Figure S5). The composite color of these candidates appears white in a topographically low  
292 area, indicating basaltic materials confined in topographic depression. They were considered as  
293 basalts that erupted in the same way as nearby maria, and hence we carefully excluded these  
294 areas from our exposure identification. These locations were included as mare exposures  
295 (marked with M and ID number) and compared to other pyroxene exposures later.

296 The FeO contents of the pyroxene exposures are probably a mixture of mare and highland  
297 materials. As shown in Figure 4c, the candidates are distributed continuously between highland  
298 and mare materials. Some of their FeO contents exceed even 12 wt.% and are higher than noritic  
299 lunar rocks (Lucey et al., 1998). However, the values are slightly lower than that of maria.  
300 Similarly, their TiO<sub>2</sub> contents range from 0.5 to 1.3 wt. %, varying between mare and highland  
301 materials. Thus, the compositional characteristic of these pyroxene-like exposures indicates a  
302 mixture of highland anorthosite and mare-like basaltic material.

303 The absorption peaks additionally support a mixture of basaltic material within the  
304 anorthositic crust around LGA2. In Figure 4d, the majority of both 1000- and 2000-nm peak  
305 positions are distributed out of LCP but in a range similar to HCP. While both 1000- and 2000-  
306 nm peak wavelengths are shorter than those of the majority of synthetic clinopyroxene and some  
307 of them are similar to LCP, the majority of their distribution is laid within the same range as  
308 maria. Furthermore, many of them possess almost the same peak positions as the maria in this  
309 region, indicating a mixture of basaltic material as the FeO and TiO<sub>2</sub> trends show.

## 310 3.3 LGA20

311 LGA20 possesses brighter exposures, particularly in the southern area of its center, in the  
312 composite map, and we found 13 candidates in total. The areas inside Edison and Lomonosov  
313 craters are covered by maria (Figure 1), so we selected 8 fresh craters on the mare region as the  
314 reference of basalt.

315 The FeO and TiO<sub>2</sub> contents are distributed between mare and highland materials  
316 continuously in the same manner as LGA2. As shown in Figure S3, the FeO content around  
317 LGA20 ranges from 8 to 10 wt % on average, which is much higher than that of the typical  
318 highland. Some of the locations near the rim of Edison crater exhibit FeO of 10 % or even  
319 higher. The variation of TiO<sub>2</sub> content is also similar to that around LGA2 and stays in the range

320 of 0.5 – 1.5 wt%. On the other hand, the TiO<sub>2</sub> content in the mare region is more widespread  
321 than that around LGA2 because the mare inside Lomonosov crater has more abundant TiO<sub>2</sub> (see  
322 Figure S4), possibly because of a temporal change of magma compositions in this region or  
323 contamination of Edison's mare by low-FeO highland material (Giguere et al., 2003).

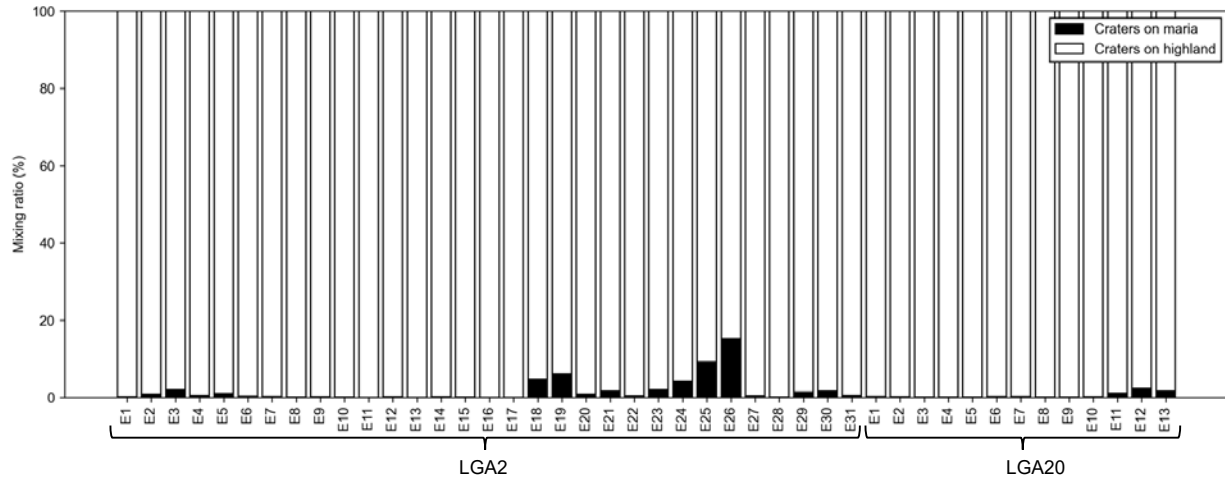
324 The 1000- and 2000-nm pyroxene absorption peaks also manifest the existence of HCP  
325 around Edison crater. The discovered pyroxene exposures have absorption peaks in the range of  
326 clinopyroxene (Figure 4). The main difference from LGA2 is that the peak wavelengths are a  
327 little shorter than those of mare. This could be due to a different extent of contamination by  
328 numerous ejecta or a compositional difference between maria and pyroxene exposures. Roche  
329 and Edison craters are Nectarian and Pre-Nectarian aged, respectively, and the excavation event  
330 by Roche crater predates that by Edison. Thus, a mixture of highland material is more enhanced  
331 around LGA20 than LGA2.

### 332 3.4 Possible sources of discovered basaltic exposures

333 Our spectral analysis found that the peripheries of LGA 2 and 20 possess abundant  
334 exposures with high FeO and HCP-like adsorptions. These basaltic spectra and compositions  
335 suggest ancient excavation of basaltic LGA materials by Roche and Edison craters. However,  
336 this discovery might also be attributed to other causes: ejecta from a mare, impact melt,  
337 pyroclastic material, and mafic melt trapped within the crust during the magma ocean  
338 solidification.

339 The first possibility of basaltic ejecta from mare regions is excluded by ejecta distribution  
340 modeling. The regions where basaltic exposures are discovered contain some small maria that  
341 also have HCP and high FeO abundance. One of the end members of the material mixture  
342 indicated by our spectral analysis could be the deposition of basaltic mare material ejected from  
343 craters on small maria after the Roche/Edison formation. To estimate this effect, we integrate the  
344 empirical relationship between ejecta thickness and distance from a crater (McGetchin et al.,  
345 1973; Melosh, 1989) with one of the most detailed lists of craters with a diameter of 1 km or  
346 larger (Wang et al., 2021). Figure 5 shows the ratio of ejecta from mare regions (red lines in  
347 Figure 1c and e). As obviously shown, the ejecta deposited on the pyroxene candidates is  
348 dominated by highland ejecta, and the ratio of ejecta from mare craters is always lower than 20  
349 wt. %. Such a low mixing ratio makes the FeO contents as low as highland material, inconsistent  
350 with the observed values. Therefore, the observed HCP exposures cannot be explained by ejecta  
351 from basaltic surface units.

352



353

354 Figure 5. The ratio of ejecta deposited at each HCP exposure around LGA2 and 20. The black  
 355 and white boxes show the contribution of ejecta from craters on mare and highland, respectively.

356 The impact melt is also unlikely for the source of these exposures. Once a crater-forming  
 357 impact occurs, this energetic event melts the target material. Previous remote-sensing data of  
 358 impact melt show absorption peaks consistent with HCP (e.g., Moriarty & Pieters, 2018).  
 359 However, topography around the pyroxene exposures is not consistent with impact melt. While  
 360 impact melt often forms pond-like morphology, topographic depression is excluded from the  
 361 exposure candidates as described above. Also, areas nearby the candidates do not have  
 362 morphology specific to impact melt, like flow features and cooling fractures, as seen in impact  
 363 melt around other craters (e.g., Krüger et al., 2016). Moreover, the mass fraction of melt product  
 364 in ejecta would be less than 10 wt % based on the empirical formula for gabbroic anorthosite  
 365 (Melosh, 1989) and numerical simulations (Liu et al., 2022), which is inconsistent with the  
 366 observed FeO content.

367 In addition, the observed spectra reject the possibility that the exposures originated from  
 368 pyroclastic deposits. Similar to dark mantle deposits identified on the Moon (e.g., Besse et al.,  
 369 2014), this high-FeO material could be composed of pyroclastic glasses emplaced by explosive  
 370 volcanic eruptions. By using Clementine multispectral images, Giguere et al. (2003) categorize  
 371 the southern region of Edison crater as dark mantle deposits of probably pyroclastic origin based  
 372 on its low albedo. Such pyroclastic material could appear to have moderately high FeO  
 373 abundances via our estimation from multiband reflectance. This is because the empirical formula  
 374 between reflectance and FeO is not calibrated for glasses, possibly enhancing the FeO abundance  
 375 at dark mantle deposits unreasonably. However, the peak positions of dark mantle deposits in the  
 376 1000- and 2000-nm bands range above 990 nm beyond 2000 nm (e.g., Besse et al., 2014;  
 377 Kumaresan & Saravanavel, 2022). These ranges are outside the continuous distribution of  
 378 pyroxenes in Figure 4.

379 The final alternative source is mafic melt trapped within the crust, but this seems unlikely  
 380 as well. Several studies on lunar hyperspectral data have identified HCP mixture in highland  
 381 craters, which perhaps suggests the existence of mafic liquid trapped within the anorthositic  
 382 cumulates during the lunar magma ocean solidification (Ogawa et al., 2011; Yamamoto et al.,  
 383 2015). Numerical simulation by Piskorz & Stevenson (2014) also suggests that mafic melt

384 cannot wholly be expelled from the lunar crust shallower than 5 km during the formation of  
385 floating anorthosite cumulates. On the other hand, a global survey of HCP by Yamamoto et al.  
386 (2015) shows that no craters with diameters less than 6-10 km possess HCP. Their result implies  
387 that the uppermost crustal layer within a depth of 1 km is dominated by LCP rather than HCP.  
388 To exclude this possibility, our analysis focused on craters with diameters of 8 km at maximum,  
389 and the majority of them are smaller than a few hundred meters.

390 In summary, the pyroxene exposures analyzed in our study are the most likely to  
391 originate from basaltic material, which does not exist on the present lunar surface as either maria  
392 or impact melt. In particular, all the hypotheses above fail to explain the difference in the  
393 existence of HCP exposures between Rowland and Roche craters, and another hypothesis to  
394 bring basaltic material to the region is necessary.

395

#### 396 **4 LGA excavation indicated by gravity anomaly**

397 A possible source that could be attributed to the spectral difference among Rowland,  
398 Roche, and Edison craters is the subsurface LGA material excavated by the analyzed craters. To  
399 investigate if these HCP exposures came from the subsurface ancient dikes or not, we next  
400 compare cratering simulation results and lunar gravity data. Interestingly as seen in Figure 1, the  
401 linear structures in the lunar gravity gradient map have different characteristics inside craters;  
402 LGA1 appears terminated at the rim of Rowland crater, but LGA2 penetrates through the Roche  
403 crater. Both craters have similar diameters of around 160 km. Therefore, we simulate the  
404 subsurface modification and excavation by these craters and calculate variations of gravity  
405 anomalies after the crater formations to test the LGA excavation hypothesis.

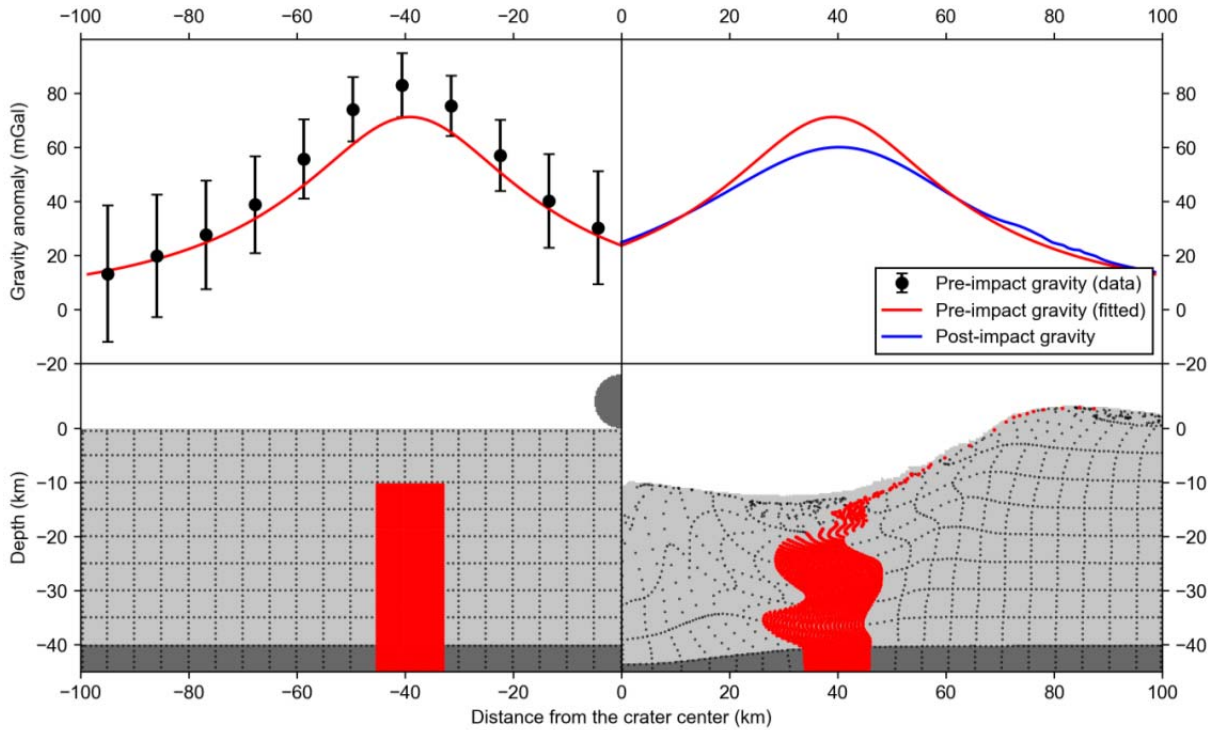
406 Our gravity modeling consists of two parts; (i) estimation of possible subsurface  
407 structures from the GRAIL gravity data and (ii) simulation of gravity change due to excavation  
408 and deformation of the subsurface structure by the crater formations. Due to the non-uniqueness  
409 of gravity inversion, a certain variety of subsurface structures satisfies the observed gravity data.  
410 Thus, we first prepare a set of intrusion shapes from gravity data outside the featured crater  
411 where crustal deformation due to impact is assumed to be negligible. Various density differences  
412 between the intrusion and surrounding crust are taken. Next, we simulate the subsurface  
413 modification for every pattern of the shape with the iSALE shock physics code (Amsden et al.,  
414 1980; Collins, 2014; Collins et al., 2011; Collins et al., 2004; Ivanov et al., 1997; Melosh et al.,  
415 1992; Wünnemann et al., 2006) and gravity structure above the crater interior after its formation.  
416 Finally, we compare the simulation and observed data, and discuss the cross-cutting relationship  
417 between LGAs and the craters.

#### 418 **4.1 Modeling procedure**

419 We begin with preprocessing of Bouguer gravity data around the craters by filtering  
420 specific wavelengths and rotating the coordinates. In the same manner as Andrews-Hanna et al.  
421 (2013), we first make a band-passed Bouguer anomaly map. From a lunar Bouguer-corrected  
422 gravity model of GRGM1200A\_BOUGUER (Lemoine et al., 2014), we extract the spherical  
423 harmonics coefficients with degrees of 50-300 to filter out the noise effect and long-wavelength

424 structures. The filtered gravity map was next rotated using spherical harmonic transformations so  
425 that LGA is located on the lunar equator. This allows us to apply a Cartesian coordinate in our  
426 latter analysis because the scale of interest is much smaller than the radius of curvature of the  
427 Moon (Liang & Andrews-Hanna, 2022).

428         The possible patterns of LGA structures before cratering are estimated by fitting a  
429 rectangular density anomaly to the gravity data outside the crater, assuming that the subsurface  
430 structures of LGA continue both outside and inside the crater before its formation. We regard the  
431 average of LGA values outside the crater as typical pre-cratering gravity. It should be noted here  
432 that the gravity profile perpendicular to LGA was averaged by aligning peak gravity horizontally  
433 because LGA is not completely linear. Then, we fit gravity values from an intrusive subsurface  
434 body with a uniform density to the averaged LGA profile. The density of magma intrusion is as  
435 high as that of the mare basalt (Kiefer et al., 2012), but the source of gravity could be a swarm of  
436 dikes, which reduces the density difference rather than a single giant dike (Andrews-Hanna et al.,  
437 2013). Thus, the density difference between the intrusion and crust varies from 200 to 1000  
438  $\text{kg/m}^3$ . Owing to the non-uniqueness of the gravity inversion, the shape of the intrusive body has  
439 to be assumed in addition. In principle, the LGA value can be fitted by other complex shapes,  
440 such as T-like prisms, but Liang & Andrews-Hanna (2022) has revealed that changing the  
441 assumed shape does not significantly improve the fitting. Therefore, we assume the simplest  
442 tabular intrusion hereafter, as Andrews-Hanna et al. (2013). A Bayesian approach by Andrews-  
443 Hanna et al. (2013) indicated that the probability of a top depth of less than 5 km is not zero. On  
444 the other hand, no mafic spectrum is observed just above the LGA, meaning that LGA material  
445 does not reach the surface directly. Thus, we set a non-zero top depth at every 2 km interval.  
446 Then, with the assumed density and top depth of a tabular intrusion, its width and center position  
447 are treated as fitting parameters (Figure 6). It should be noted that the root of the intrusion is  
448 placed at the Moho boundary. Because magma is negatively buoyant everywhere above the lunar  
449 Moho, it is difficult to stall the dike without any pressure from magma in the mantle (Wilson &  
450 Head, 2017).



451

452 **Figure 6.** An example of our LGA modification simulation. The left and right figures show the  
 453 result before and after cratering, respectively. The upper and bottom figures show the gravity  
 454 profile perpendicular to LGA and the subsurface material distribution, respectively. The origin of  
 455 the x-axis corresponds to the crater center. In the top-left figure, the gravity anomaly from a  
 456 rectangular body (red line) is fitted to the averaged gravity profile (black points). In the bottom  
 457 left figure, the corresponding rectangular intrusion is shown in red. The light and dark pixels are  
 458 the crust and mantle. The dark semicircle in the bottom-left figure is the projectile. The blue line  
 459 in the top right figure shows the gravity profile from the modified intrusion. The density  
 460 difference and top depth assumed in this figure are  $400 \text{ kg/m}^3$  and 10 km, respectively.

461

462 The subsurface material movements by a meteoroid collision were numerically traced by  
 463 a crater-forming simulation. In this work, we use the iSALE-2D shock physics code (Amsden et  
 464 al., 1980; Wünnemann et al., 2006), which is based on the SALE hydrocode solution algorithm  
 465 (Amsden et al., 1980). To simulate hypervelocity impact processes in solid materials, SALE was  
 466 modified to include an elastoplastic constitutive model, fragmentation models, various equations  
 467 of state (EoS), and multiple materials (Ivanov et al., 1997; Melosh et al., 1992). More recent  
 468 improvements include a modified strength model (Collins et al., 2004), a porosity compaction  
 469 model (Collins et al., 2011; Wünnemann et al., 2006), and a dilatancy model (Collins, 2014). In  
 470 our simulation, a dunite projectile with a radius of 5 km collided on the lunar surface at the speed  
 471 of 20.9 km/s. This impact speed was the same as the median speed of an asteroid collision with  
 472 the Moon during the Late Heavy Bombardment epoch (Bottke et al., 2012). The target was  
 473 assumed to be a two-layered surface composed of basalt crust and dunite mantle. As a result, a  
 474 crater with a diameter of 160 km was formed in our simulation. All the parameters are

475 summarized in Table S2. In addition, it should be noted here that the choice of materials does not  
476 make a substantial difference, as reported by (Melosh et al., 2013; Miljković et al., 2015).

477 The gravity before and after the collision was calculated by integrating the iSALE tracers,  
478 which are originally located within the fitted tabular body. The positions of tracers are moved by  
479 cratering within a vertical plane that contains the original tracer location and crater center.  
480 Because our cratering simulation is axisymmetric, we calculate a cross-section of the LGA body  
481 at each azimuth and integrate them to determine the positions of tracers in cylindrical  
482 coordinates. Each tracer is treated as a rectangular box with the assumed density, and its gravity  
483 anomalies were summed up to make a gravity map after the crater formation. In particular, the  
484 gravity value within a distance of 15 km from the intrusion center changed after crater formation  
485 and was reduced by 30 mGal at most, as demonstrated in Figure 6. Thus, we focused on the  
486 gravity within this narrow region inside the crater. Note that our simulation treats a  
487 homogeneous crust because calculation only with the iSALE tracers is sufficient to estimate  
488 gravity change due to the subsurface modification. Although the density gap between the LGA  
489 intrusion and surrounding crust causes the reflection of shock waves and could suppress the  
490 modification beneath the crust, we confirmed that such a density gap little affects the overview at  
491 all. Even if the density gap is set over  $800 \text{ kg/m}^3$ , the difference in resultant gravity between  
492 homogeneous and heterogeneous crust models is less than 5 mGal (Figure S6).

493 Another contribution to the gravity inside craters comes from porosity change during the  
494 crater formation. Soderblom et al. (2015) show that the Bouguer anomaly of lunar complex  
495 craters has a negative value on average, implying that the porosity beneath the crater is higher  
496 than the crust due to the fracturing by shock waves. Their analysis also reveals that the average  
497 gravity inside the crater has a significant variation among craters, ranging from +10 to -40 mGal.  
498 These wide-spreading values originate from the pre-impact porosity beneath the crater because  
499 the impact can also close pores inside highly fractured material (Milbury et al., 2015). In  
500 addition, the gravity anomaly could be variable inside the crater. For example, if the initial  
501 porosity is high, pore closure is enhanced more in the central region of the crater than the outer  
502 area, resulting in a high Bouguer anomaly around the crater center. This could affect the gravity  
503 profile in our analysis, especially in the case of LGA1, whose direction is nearly toward the  
504 center of Rowland crater. To include these pore creation and destruction in our simulation, we  
505 include the dilatancy model to consider a variety of the initial porosity effect, following the  
506 parameters presented by Collins (2014), Milbury et al. (2015), and Miljković et al. (2021) (Table  
507 S2). The LGA gravity inside the crater is weaker than that outside for both Rowland and Roche  
508 craters, suggesting that the initial porosity was low. Milbury et al. (2015) have already shown  
509 that an initial porosity of 6.8 % generates positive gravity values inside a 160-km-sized crater.  
510 Thus, we set the initial porosity for various values from 0 to 8 %. Next, we add the various  
511 gravity profile from dilatancy to that from the LGA modification. After binning the simulated  
512 gravity distribution to the same resolution as the data, we then find the best-fit dilatancy model to  
513 minimize the residuals of our simulation from the data. For this comparison, we use pixels that  
514 are located inside the crater and within 10 km of the LGA center, corresponding to the area  
515 where the gravity is affected by both impact processes. Finally, we take the gravity signature  
516 with the best-fit dilatancy as the best-gravity model for each case of assumed parameters.

517 4.2 Rowland crater on LGA1

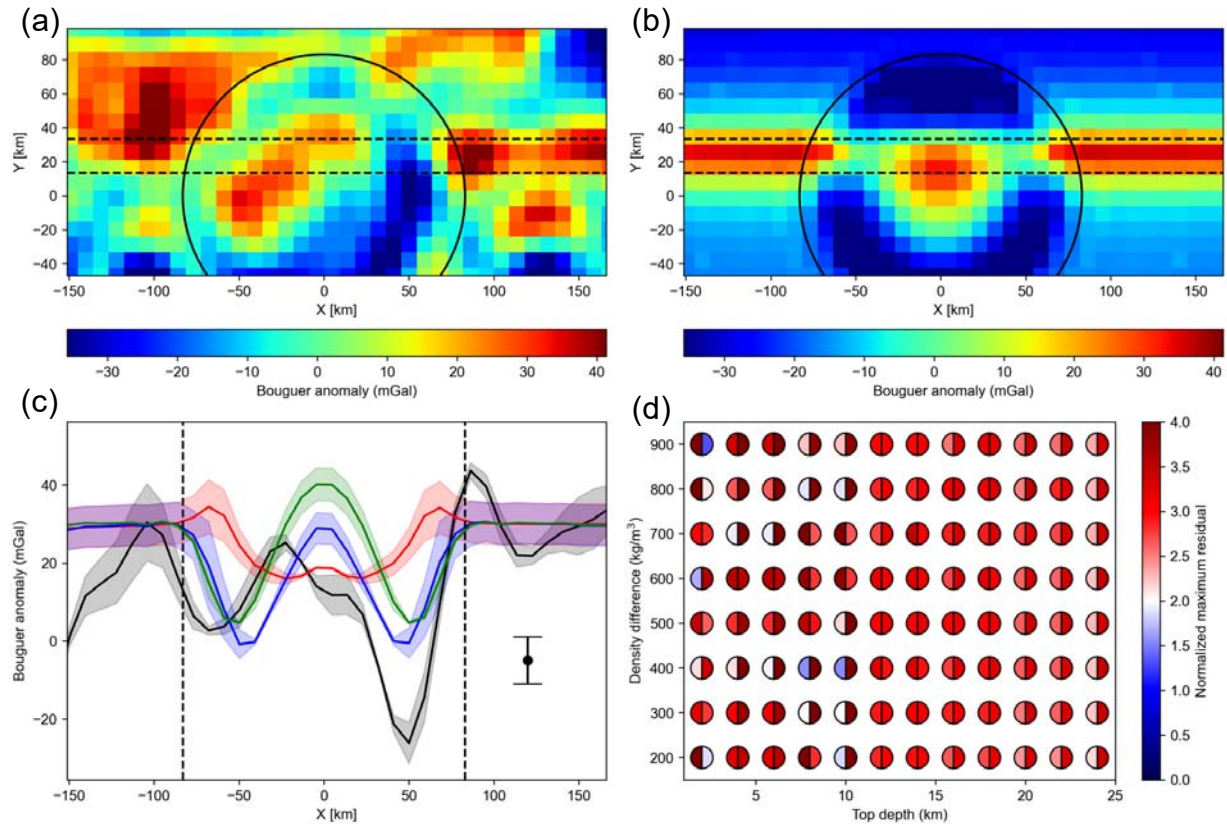
518 Our numerical simulation reveals that LGA1 has not penetrated Rowland crater. The  
519 simulated gravity profile was never consistent with the observed one inside the Rowland crater,  
520 especially the substantial gravity gap between the rim and center. The gravity anomaly and  
521 gradient data show that the gravity inside Rowland crater drops for more than 70 mGal adjacent  
522 to the apparent LGA1 (Figure 7c) and appears terminated at the crater rim in the gravity gradient  
523 map (Figure 1b). This gravity drop is much larger than that by the excavation and deformation in  
524 the crater formation. Figure 7b shows the case that the density difference, top depth, and initial  
525 crustal porosity are assumed to be  $400 \text{ kg/m}^3$ , 10 km, and 2.0 % respectively. Figure 7c  
526 demonstrates that the gravity value after the collision decreases inside the crater. The Bouguer  
527 anomalies within the area surrounded by two black dashed lines in Figure 7a and b are averaged  
528 along the y-axis (the black, red, blue, and green lines in Figure 7c). The simulated value goes up  
529 and down qualitatively in the same manner as the observed data. However, the LGA-like gravity  
530 still appears to continue throughout the Rowland crater because the gravity drop nearby the rim  
531 is only about 30 mGal and a factor of two less than the observed drop (Figure 7b).

532 The discrepancy between our numerical simulation and the observed gravity anomalies is  
533 caused by a remaining root of the intrusion. To account for the high gravity at the central part of  
534 Rowland simultaneously, the best-fit dilatancy model makes the gravity drop of only 15 mGal  
535 nearby the rim as shown by the green line in Figure 7c. On the other hand, the LGA modification  
536 decreases the Bouguer gravity by only 15 mGal in the crater for this case. As demonstrated in  
537 Figure 6, the crater formation is not able to destroy all the structures of the intrusion. Therefore,  
538 the root of the intrusion still remains beneath the simulated crater, failing to explain the complete  
539 termination of LGA at Rowland's rim in the observed data.

540 Any simulated gravity profiles cannot describe the specific gravity signature inside the  
541 Rowland crater, implying that LGA1 did not pre-exist before the Rowland formation. To make  
542 sure of this finding, we investigate all the sets of assumed density and top depth. We calculated  
543 differences in the average gravity profiles between observation and simulation (black and blue  
544 lines in Figure 7c). The gravity just above the LGA location is non-uniform, which would be an  
545 original variation of LGA before the crater formation. Thus, the difference was normalized by a  
546 standard deviation of LGA gravity (black error bar in Figure 7c). To examine the similarity  
547 between the gravity value and profile shape quantitatively, we focus on the normalized  
548 difference at the local gravity minimum and maximum inside the crater. In Figure 7d, the  
549 normalized differences between the observation and simulation are shown for all the assumed  
550 parameter sets. Although the local maximum can be reproduced within two standard deviation  
551 ranges with a couple of parameter sets, the difference at the local minimum is always larger than  
552 three standard deviations. This implies that the great gravity gap next to the terminator of LGA  
553 cannot be attributed to the cratering excavation and is evidence that LGA1 did not continue  
554 beyond the Rowland rim even before the crater formation.

555

556



557

558 **Figure 7.** Comparison between simulations and the observed data. (a) The Bouguer anomaly  
 559 map around Rowland crater. The solid black line shows the rim position. The area between the  
 560 two black dashed lines is the area used for the comparison. Note that the coordinate is rotated to  
 561 make the LGA direction parallel to the x-axis. (b) An example of a simulated Bouguer anomaly  
 562 map when the density difference, top depth, and initial crustal porosity are assumed to be 400  
 563  $\text{kg/m}^3$ , 10 km, and 2.5 %, respectively. (c) The averaged gravity profile within the compared  
 564 area. The observed data is shown in the black line. The red, green, and blue lines show the  
 565 gravity change by the LGA modification, porosity change, and the sum of these two effects. The  
 566 shaded areas correspond to a standard deviation range within the compared area along the y-axis.  
 567 The black error bar shows a standard deviation of the LGA gravity outside the crater. (d) The  
 568 normalized difference at the local maximum and minimum within the crater. The colors in the  
 569 right and left semi-circles show the values at the local minimum and maximum, respectively.

570

### 571 4.3 Roche crater on LGA2

572 On the contrary, our simulation successfully reproduces gravity signatures similar to the  
 573 LGA2 values inside the Roche crater. As shown in Figure 1d and 8a, the gravity inside the  
 574 Roche is weaker than that outside but a linear feature extends across the Roche crater. This  
 575 feature is also seen in our numerical simulation. Figure 8b and c demonstrate an example case  
 576 simulated under the same assumption of the density difference and top depth as Figure 7. The  
 577 excavation and deformation of LGA blur the linear feature, but the remaining root of LGA

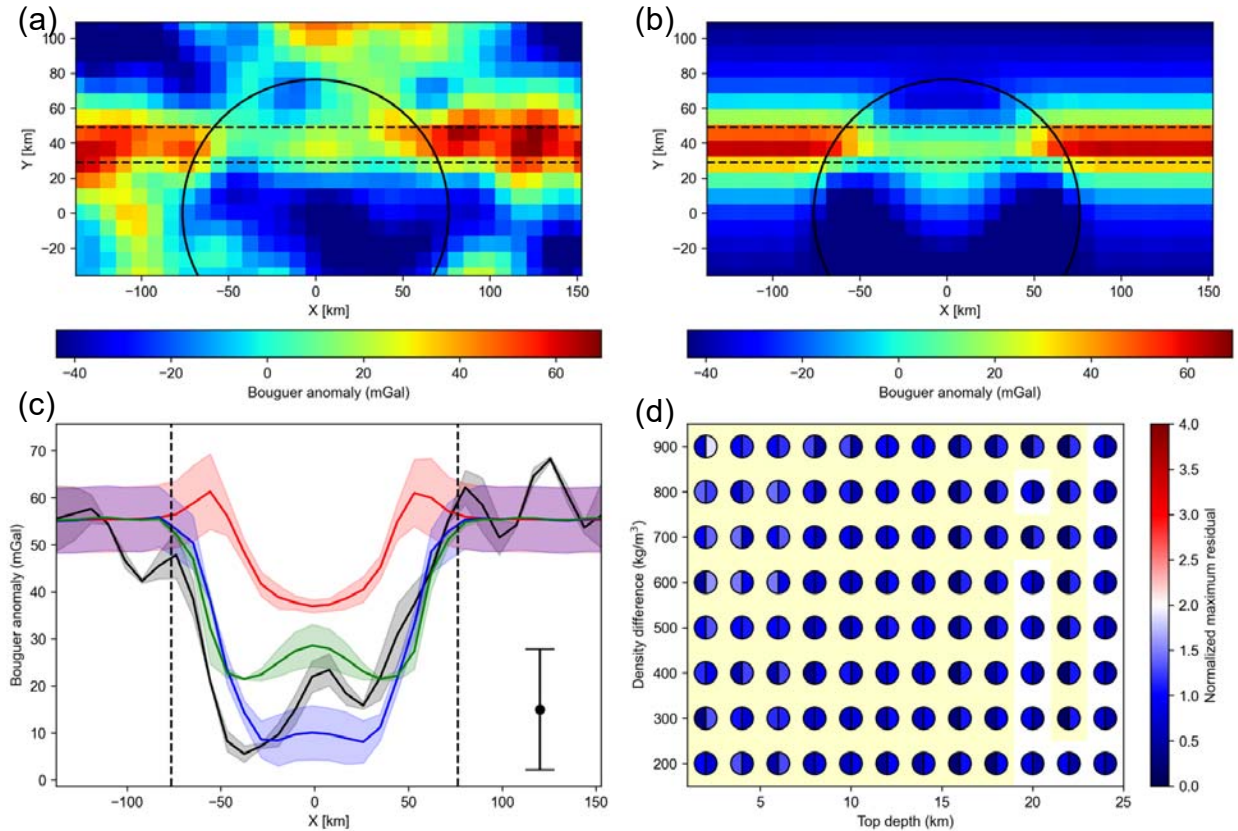
578 beneath the excavation depth of Roche still appears as a continuation of LGA. The average  
579 gravity decrease of about 50 mGal inside Roche crater is not as extreme as that inside Rowland  
580 crater. As shown in Figure 8c, this moderate decrease can be attributed to the sum of the LGA  
581 modification and porosity production due to the Roche formation. This comparison between  
582 simulated and observed gravity implies that LGA2 was affected but not entirely destroyed by the  
583 crater formation.

584 The comparison between the simulation and data for all the parameter sets confirms the  
585 effect of the impact cratering on LGA2. Figure 8c shows that the averaged gravity within Roche  
586 crater floor has a variation with a range of 20 mGal. Because the LGA2 gravity outside Roche  
587 crater also has a variation, we investigate whether the simulated profile matches the data at the  
588 local maximum and minimum in the same way as LGA1. Figure 8c depicts that the gravity  
589 signature always agrees with the observation within 1.5 standard deviations. Thus, the porosity  
590 and intrusion modification well explains the LGA2 gravity decrease inside Roche crater.

591 Figure 8d also implies that the favorable top depth of the intrusion is shallower than 22  
592 km. As Figure 8c demonstrates, the intrusion body at the deep area is modified but still remains  
593 in almost the same position. The gravity decrease by the LGA modification is hence less than 5  
594 mGal if the whole intrusion exists deeper than 22 km before the impact. In addition, the gravity  
595 decrease is limited to the locations nearest to the crater center (Figure 8c), where the depth of the  
596 excavated and modified region is the deepest on LGA2. This value is too small to explain the  
597 observed gravity decrease of 50 mGal even with negative gravity from porosity production  
598 because the observed gravity decreases inside lunar craters with a size similar to Roche range of  
599 less than 40 mGal (Soderblom et al., 2015). Thus, cases for a top depth deeper than 22 km are  
600 unlikely to explain the observation.

601

602



603  
 604 **Figure 8.** Comparison between simulations and the observed data. (a) The Bouguer anomaly  
 605 map around Rowland crater. The solid black line shows the rim position. The area between the  
 606 two black dashed lines is the area used for the comparison. (b) An example of a simulated  
 607 Bouguer anomaly map when the density difference, top depth, and initial crustal porosity are  
 608 assumed to be  $400 \text{ kg/m}^3$ , 10 km, and 2.0 %, respectively. (c) The averaged gravity profile  
 609 within the compared area. The observed data is shown in the black line. The red, green, and blue  
 610 lines show the gravity change by the LGA modification, porosity change, and the sum of these  
 611 two effects. The shaded areas correspond to a standard deviation range within the compared area  
 612 along the y-axis. The black error bar shows a standard deviation of the LGA gravity outside the  
 613 crater. (d) The normalized difference at the local maximum and minimum within the crater. The  
 614 colors in the right and left semi-circles show the values at the local minimum and maximum,  
 615 respectively. The color behind the circle is yellow when the necessary gravity decrease solely  
 616 from the porosity change is larger than 40 mGal.

## 617 5 Discussion on each LGA history

### 618 5.1 LGA1

619 The spectral and gravitational features around LGA1 imply that Rowland crater did not  
 620 excavate LGA1, possibly meaning that the intrusion of LGA1 postdates the Rowland crater. As  
 621 demonstrated in our gravity simulations, the observed gravity profile with the substantial gravity  
 622 drop does not match the assumption that Rowland crater obliterates the pre-existing LGA1.  
 623 Together with the lack of HCP exposures in the periphery, these results confirm that the  
 624 magmatic intrusion of LGA1 did not exist beneath the area where Rowland crater occupies at

625 present. There are two possibilities attributable to our result; the Rowland crater was formed  
626 coincidentally just next to the edge of LGA1, or LGA1 was formed after Rowland crater. Although  
627 the first hypothesis cannot be ruled out, the probability of such a “lucky” impact is tiny.  
628 Multiplying the highland crater density (Head et al., 2010; Heyer et al., 2023) by the area where  
629 a crater may be located with its rim overlapping the terminator of LGA1 within the gravity  
630 resolution, the expectation of the number of 160-km-sized craters in contact with LGA1 is less  
631 than 0.01. Therefore, the more plausible scenario is that the LGA1 magma started to intrude into  
632 the crust after the crater formation but terminated at the rim of Roche crater.

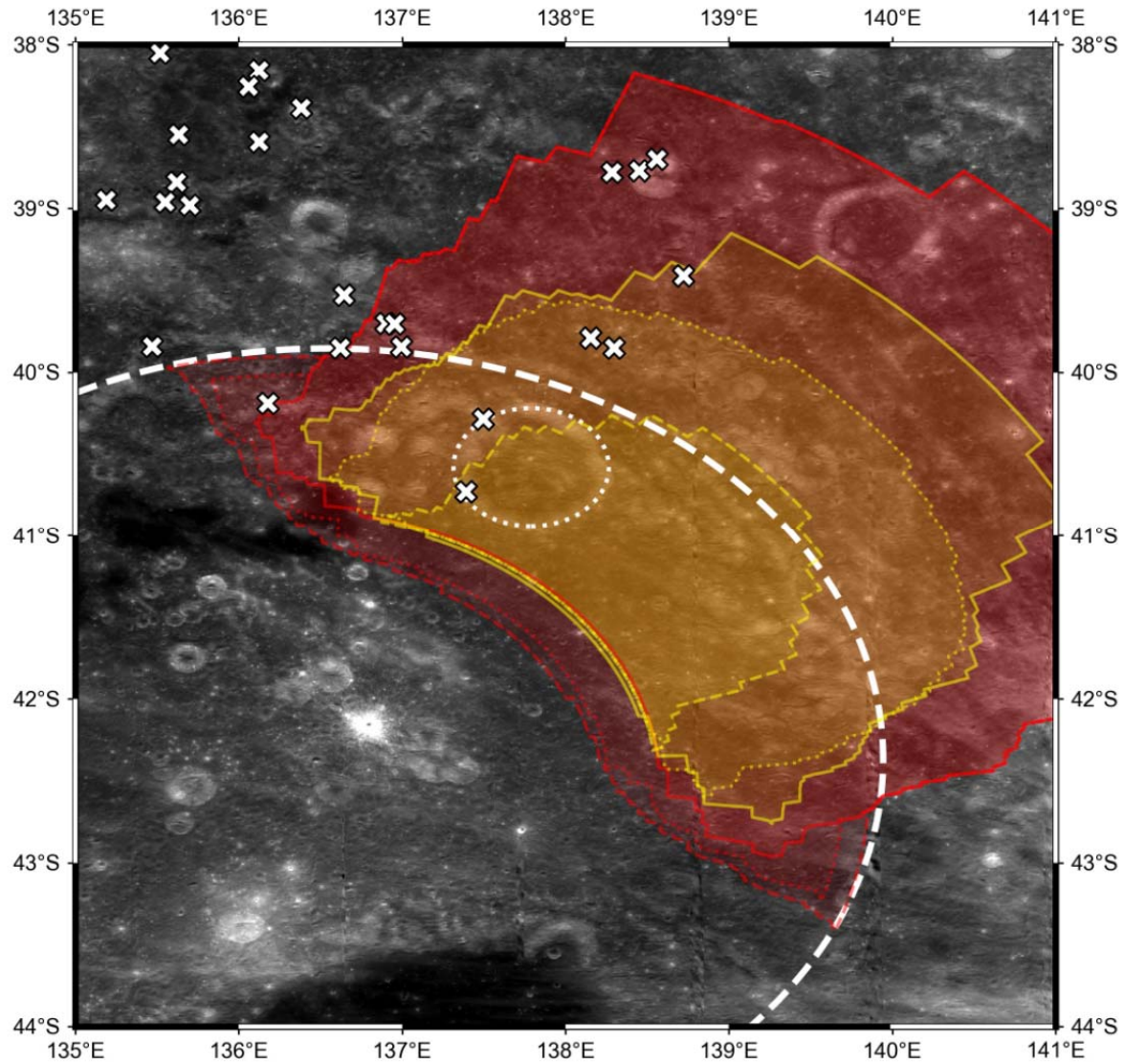
633 The termination of LGA1 at the rim of Rowland crater was perhaps caused by Rowland’s  
634 topography. The orientation of dike intrusion is determined by the stress state of the media and  
635 follows the direction perpendicular to the maximum tensile stress at the time of its formation  
636 (e.g., Watanabe et al., 2002). In particular, a crater-like round depression generates a stress field  
637 in which a crack-opening direction favors a circular orientation. As the demonstration of a  
638 magma ascent beneath lunar floor-fractured craters by Michaut et al. (2020), unloading by a  
639 crater bends the trajectory of dikes beneath the crater, and magma ascends towards the rim of the  
640 above crater. In Figure 1, a negative gravity gradient of LGA does not last into the Rowland  
641 crater but curves along the rim from the terminated point. Similar ring dike structures are  
642 apparent around other impact basins like Orientale (Andrews-Hanna et al., 2018). A ring fault  
643 made by a giant basin formation is regarded as a path for magma ascent. Although the size of  
644 Rowland crater is smaller than craters accompanied by such a tectonic fault, the paleo stress field  
645 caused by Rowland’s unloading could bend the direction of magma intrusion around the rim of  
646 Rowland, resulting in an abrupt termination of the LGA1 gravity signature.

647 The above discussion on the LGA1 formation scenario suggests a new estimate of the  
648 LGA1 formation age and, furthermore, the timing of the ancient lunar expansion. Previous works  
649 have argued that the age of LGA1 is older than the Nectarian age in various ways. Sawada et al.  
650 (2016) estimated by crater-counting that the surface age around LGA1 is  $4.20^{+0.02}_{-0.03}$  Ga,  
651 corresponding to pre-Nectarian age. However, their argument does not agree with the cross-  
652 cutting relationship found by our analysis, showing that the surface age on LGA1 does not  
653 represent the timing of subsurface intrusion. In addition, Liang & Andrews-Hanna (2022) argue  
654 that LGA1 is likely to postdate the Rowland formation. They attribute the apparently abrupt  
655 termination of LGA1 at Rowlands’ rim to a reduction of the density contrast between the crust  
656 and LGA1 intrusion by the crater-forming shock waves, but their hypothesis is ruled out by our  
657 numerical results considering the porosity change. On the other hand, they also point out that the  
658 LGA1 gravity remains but becomes a little ambiguous beneath the Upper-Imbrium-aged  
659 Schjellerup crater. This feature is similar to our numerical simulations of crater obliteration on  
660 LGA1 and 2. Therefore, the LGA1 formation started after the Nectarian age and probably ended  
661 by the Upper-Imbrium age. This age is the youngest age estimation of LGAs on the Moon at  
662 present. From the apparent cross-cutting relationships of LGAs with two giant basins, the  
663 Crisium and South-Pole-Aitken basins, Andrews-Hanna et al. (2013) constrain that the LGAs  
664 were formed within the pre-Nectarian to early Nectarian time frame. Our analysis geologically  
665 implies that the lunar expansion accompanied by LGA formations continued even later than the  
666 Nectarian age as predicted by various thermal modeling of the Moon (U et al., 2022; Zhang et  
667 al., 2013a, 2013b).

668 5.2 LGA2

669 Our gravity simulation poses a constraint on the LGA2 formation age and is consistent  
670 with our discovery of HCP exposures in the periphery. Consistency between our gravity  
671 simulations and the observed Bouguer anomalies validates the assumption of intrusion before  
672 cratering, indicating that the Roche-forming impact postdates the magmatic intrusion of LGA2.  
673 Roche is a Nectarian-aged crater (Wilhelms & El-Baz, 1977), and the absolute age of a light  
674 plain within it is estimated to be 3.91 Ga from the crater size-frequency distribution (Hiesinger et  
675 al., 2013). Therefore, together with its formation later than the South-Pole-Aitken basin  
676 (Andrews-Hanna et al., 2013), our analysis confirms that the LGA2 formation occurred within  
677 the pre-Nectarian to Nectarian age. This cross-cutting relationship also agrees that the discovery  
678 of HCP exposures possibly originated from ancient magma intrusion excavated by Roche crater.  
679 The predicted excavation depth of Roche is about 16 km and comparable to the maximum value  
680 of the preferable top depth of intrusion in our analysis. Thus, the ejecta from Roche crater could  
681 contain a certain portion of LGA material. In fact, most of the discovered HCP exposures in our  
682 spectral analysis are located within the continuous ejecta region (Melosh, 1989; Moore et al.,  
683 1974).

684 On the other hand, the majority of non-mare HCP exposures that we found are not laid  
685 within the area predicted in our axisymmetric simulations. The RGB-composite and FeO maps  
686 show that the basaltic materials are identified in the northern area of Roche crater (Figures S1  
687 and S3). However, the LGA materials traced in our simulation are deposited mainly in the  
688 northern-eastern area. Figure 9 shows the distribution of LGA materials that are expected to  
689 deposit on the surface in our simulation. Because the thickness of the top-surface mixing layer is  
690 at least 1 km (Yamamoto et al., 2015), the LGA material whose final depth from the surface is 1  
691 km or deeper is traced in this analysis (three red lines in Figure 9). The distribution depends on  
692 the assumed density and top depth. In the case of high-density assumption, because the fitted  
693 width of intrusion becomes narrow, the portion of intrusions close to the crater center decreases.  
694 Due to the decrease of excavation depth with the distance from the center, the volumetric ratio of  
695 excavated material is reduced for high-density cases (yellow area in Figure 9). The top depth is  
696 also important because the shallower the intrusion is, the more subject to the excavation (yellow  
697 lines in Figure 9). Therefore, when the shallowest and widest intrusion is assumed, the simulated  
698 ejecta distribution is the broadest and covers some HCP exposures discovered around the  
699 Roche's rim and at the wall of Roche-B crater. We estimated areas possibly covered by LGA-  
700 containing ejecta for all the assumed parameter sets. However, the prediction does not explain  
701 the whole area where the basaltic material is discovered (white crosses in Figure 9).



702

703 **Figure 9.** The deposition distribution of the LGA-containing ejecta around Roche crater. The  
 704 white dashed and dotted lines show the rim of Roche and Roche B craters, respectively. The non-  
 705 white lines show example distributions of ejected LGA material. The red area shows the case  
 706 under the assumption of the density difference and top depth of  $200 \text{ kg/m}^3$ , 2 km, respectively.  
 707 The red solid, dotted, and dashed lines show the area when the LGA tracers finally deposited at a  
 708 depth shallower than 1, 2, and 3 km are considered. The yellow area shows the case with a  
 709 density difference of  $400 \text{ kg/m}^3$ . The yellow solid, dotted, and dashed lines correspond to the  
 710 assumed top depth of 2, 6, and 10 km, respectively. The white crosses are locations of discovered  
 711 basaltic exposures flagged with E, respectively.

712

713 One hypothesis for the discrepancy between the ejecta distribution and majority of HCP  
 714 exposure positions is the Roche formation by an oblique impact. Figure S7 shows the topography  
 715 (SLDEM2015) around Roche crater and the highest positions in its rim. The topography data

716 was divided into 1-degree azimuth bins, and the highest position in each bin was extracted. To  
717 avoid contamination by ejecta from Pauli crater, the positions within its continuous ejecta region  
718 were conservatively eliminated from this analysis. After fitting an ellipse to the extracted points,  
719 we found that the Roche crater is elongated almost along the N-S direction with a semi-minor  
720 axis smaller than a semi-major axis by 7 %. According to the scaling relationships proposed by  
721 (Davison & Collins, 2022), this diameter ratio corresponds to a crater formation with an impact  
722 angle of 45 – 50 degrees. Even with such a moderate impact angle, the ejecta blankets have an  
723 asymmetry and concentrate in the impact direction (e.g., Shuvalov, 2011). Thus, the HCP  
724 discoveries centered in the northern area of Roche crater are perhaps attributed to a Roche-  
725 forming impact from the southern direction.

726 Another basaltic source of these HCP exposures, particularly in the case of nearby newly-  
727 identified mare patches (Figure S5), could be shallow subsurface magmatic intrusions whose  
728 spatial scale is too small to be resolved as LGA. From  $M^3$  spectroscopy, Corley et al. (2018)  
729 have detected some olivine exposures around LGA2. However, these detections are not present  
730 at the exact location of LGA, implying that other shallow and small magmatic intrusions are  
731 exposed by impacts. Since an ascending magma is predicted to be stalled and cooled before the  
732 eruption due to the thick crust in the lunar farside (Head & Wilson, 2017; Taguchi et al., 2017;  
733 Wilson & Head, 2017), the periphery of Roche crater is possibly the case as well. In particular,  
734 the northern region of Roche crater has some small mare patches in the low topography (Figure  
735 S5) and might have experienced volcanic activity in the past. Although the ejecta from the  
736 present maria is not the source of these exposures, HCP from these small subsurface intrusions  
737 might be contained in the regolith of this region due to the later impact mixing and is exposed at  
738 the discovered points. Nevertheless, the composition of analyzed exposures should reflect that of  
739 the ancient magma, which is a hint to know the compositions of ancient subsurface intrusions.

### 740 5.3 LGA20

741 Contrary to LGA1 and 2, the gravity signature of LGA20 is not so obvious to discuss  
742 whether the exposure candidates were excavated by Edison crater or not. The Bouguer gradient  
743 map shows an ambiguous continuation of LGA20 into Edison crater (Figure 1f). The Bouguer  
744 anomaly value inside the crater is weaker by 20 mGal than that outside it. Although this small  
745 gravity drop can be explained solely by porosity variation induced by the crater formation, this  
746 feature is qualitatively similar to LGA2, suggesting the possibility of LGA material distribution  
747 in the periphery. Considering the shallow excavation depth of Edison crater, a top depth  
748 shallower than 6 km is necessary for the ejection of the intrusive body. The floor of Edison crater  
749 and nearby Lomonosov crater is filled with lava after their formation, meaning that magma could  
750 ascend to a depth of at least a few kilometers in this region. Thus, the LGA20 intrusion could  
751 have been stalled at a shallow subsurface and excavated by Edison crater, allowing us to detect  
752 the LGA material as HCP exposures.

753 Another possible source is a mixture of ancient mare material within the regolith around  
754 LGA20. Some previous works have identified a cryptomare in the southeastern area of Edison.  
755 Geologic categorization by Giguere et al. (2003) suggests that an ancient mare is covered by a  
756 light plain deposit in the Lomonosov-Fleming region. However, the area where HCP was  
757 discovered in our analysis is outside these cryptomare regions and defined as pyroclastic  
758 deposits, which is not consistent with our hyperspectral analysis. Whitten & Head (2015a)

759 surveyed cryptomare all over the Moon and included the area nearby the Edison in the  
760 Lomonosov-Fleming cryptomare. In the central region of this cryptomare, an 8-km crater has an  
761 obvious dark halo of ancient basalt (Giguere et al., 2003). The floor of this crater has the same  
762 elevation level as that of Edison crater. Therefore, if ancient basalt was distributed uniformly  
763 within this region before the Edison formation in the pre-Nectarian age, the ancient mare could  
764 be excavated and distributed as the HCP exposures.

765

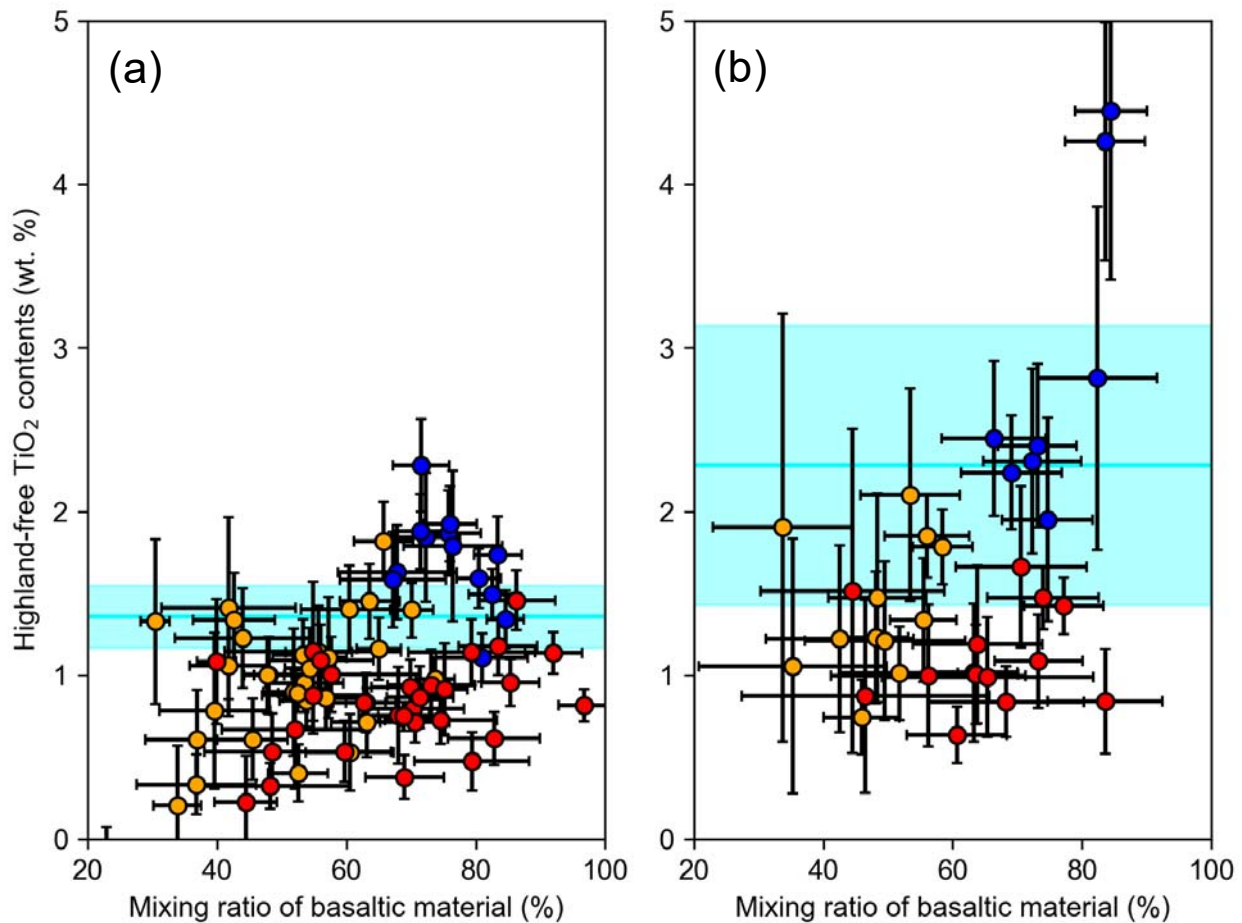
## 766 **6 Implications to ancient lunar magmatism**

767 The above analysis and discussion suggest that the HCP exposures around LGA 2 and 20  
768 contain ancient basaltic materials and possibly ejecta from the subsurface massive magmatic  
769 intrusions, enabling us to discuss the composition of magma directly related to the ancient lunar  
770 expansion. Kato et al. (2017) show that  $\text{TiO}_2$  contents varied with the age of the mare unit in the  
771 PKT region as a consequence of magma source transition. In particular, there are mare patches  
772 younger than the excavated material around both LGAs. Therefore, a comparison of titanium  
773 contents between excavated ancient material and nearby young maria would allow us to interpret  
774 the compositional evolution of volcanism in the analyzed regions. However, the discovered HCP  
775 does not directly reflect the original composition because they are possibly contaminated by  
776 highland material, as seen in Figure 4.

777 In order to determine the original compositions of the HCP exposures, we correct the  
778 highland contamination by estimating the mixing ratio from FeO contents. Assuming the FeO  
779 abundances of uncontaminated mare and highland material and the  $\text{TiO}_2$  abundance of highland  
780 material, both the highland-free  $\text{TiO}_2$  contents of excavated basaltic material and the mixing ratio  
781 of highland are estimated from our MI data analysis. The FeO and  $\text{TiO}_2$  contents of highland  
782 regolith are set at 4.0 and 0.3 wt %, respectively, following Giguere et al. (2003). The original  
783 FeO abundance of the HCP exposures is assumed in two ways: the average value of nearby  
784 maria or a typical value of lunar basalt of 18 wt %. The first assumption might underestimate the  
785  $\text{TiO}_2$  value because all the maria are contaminated by highland regolith to a certain extent. For  
786 example, the old mare inside Edison crater has an albedo higher than other maria (Figure 1),  
787 which indicates an ongoing transition from a highland-contaminated mare to a cryptomare  
788 (Giguere et al., 2003). On the other hand, the second value is higher than all the maria nearby  
789 LGAs (Figure 4) and thus gives us an upper limit of  $\text{TiO}_2$  contents. Therefore, the original LGA  
790 composition would lie between these two estimations.

791 Similarly to nearby younger maria, the corrected highland-free  $\text{TiO}_2$  contents of HCP  
792 exposures range from very-low- to low-Ti basalt, indicating a possibility of the same magma  
793 source. Figure 10 shows the mixing ratio of basaltic material and  $\text{TiO}_2$  estimated after the  
794 removal of highland contamination. Under the second assumption of FeO abundance, the mare  
795  $\text{TiO}_2$  estimation is also corrected. With both the FeO assumptions, the original  $\text{TiO}_2$  contents are  
796 always lower than 2.5 wt. % at both LGA 2 and 20. The young mare basalts are mostly  
797 distributed from 1 to 3 wt. %. It is known that lunar samples from Apollo and Luna missions  
798 show a bimodal distribution of  $\text{TiO}_2$  contents (Neal & Taylor, 1992). All the observed values at  
799 the HCP exposures and nearby maria are in the same lower class, which consists of very-low-  
800 (<1 wt. %) or low (1–6 wt. %)  $\text{TiO}_2$  basalt. This identical categorization of titanium contents

801 indicates a similar or perhaps common magma source of the LGA material (red and orange  
 802 points in Figure 10) and nearby young maria (blue points in Figure 10). In addition, Figure 10  
 803 shows the similarity of  $\text{TiO}_2$  contents between LGA2 and 20, suggesting a universal generation  
 804 of low titanium magma during the lunar expansion stage. The same low-titanium basaltic  
 805 material has also been observed in 2.03-Ga basalt samples brought by the Chang'E-5 mission (Li  
 806 et al., 2021; Tian et al., 2021). Although there is a debate on the titanium contents of the picked  
 807 basalt clasts due to their tiny size, the samples are classified as low-Ti basalts by tracking the  
 808 crystallization sequence from titanium in olivine (Zhang et al., 2022).



809  
 810 **Figure 10.** The corrected highland-free  $\text{TiO}_2$  contents around (a) LGA2 and (b) LGA20. The x-  
 811 and y- axes are the estimated mixing ratio of original basaltic material and highland-free  $\text{TiO}_2$   
 812 contents in wt. %. The orange and blue points are corrected values of exposures and maria under  
 813 the assumption of a typical FeO content of lunar basalt. The red points are corrected values in the  
 814 use of the average FeO contents of maria within the analyzed region. The cyan lines and shades  
 815 are the average and standard deviation range of the mare values without corrections.

816 If the magma sources for the LGA intrusion and nearby young maria are common, this  
 817 tiny variation of titanium abundance implies that the magma source was compositionally almost  
 818 uniform over a long period. The ages of mare patches are younger than the crater we expect to  
 819 excavate the LGA materials. At LGA 2, the maria inside Roche crater has a surface age of 1.70–  
 820 2.25 Ga. The absolute age of the small maria between Roche and Eotvos also ranges from 1.93 to

821 3.06 Ga (Pasckert et al., 2015). These mare units are younger than Roche crater, which has a  
822 light plain with an age of 3.91 Ga (Hiesinger et al., 2013). The maria around LGA 20 are  
823 categorized as units of Imbrian age (Wilhelms & El-Baz, 1977) and much younger than the pre-  
824 Nectarian-aged Edison crater. Thus, the similarity of the titanium contents between the maria and  
825 exposures implies that the composition of magma sources around these LGAs was almost  
826 uniform for 1 billion years or longer. Only a slight variation of less than 1 wt. % perhaps exists  
827 but is not so drastic as that found at the PKT region, whose  $\text{TiO}_2$  contents increased by 2–3 wt.  
828 % around 2.3 Ga (Kato et al., 2017).

829 This uniform composition around LGAs also suggests a negligible mixture of a late hot  
830 plume from IBCs in the magma source region. IBCs are thought to be laid over the core-mantle  
831 boundary and/or trapped within the mantle after the lunar mantle overturn (Hess & Parmentier,  
832 1995; Zhao et al., 2019). These IBC materials are possibly accompanied by heat-producing  
833 elements. Because the solidus of IBC is lower than that of the mantle-like olivine-orthopyroxene  
834 (Delano, 1990), IBCs could become less dense than the surrounding mantle and rise as a plume  
835 (Zhang et al., 2013a). Several numerical models have suggested that lunar hot mantle plumes  
836 from the IBC layer would happen around 2 Ga (Hess & Parmentier, 1995; de Vries et al., 2010).  
837 This mechanism has been considered as a possible source of the high-titanium magma eruption  
838 around 2 Ga, so-called Phase-2 volcanism, in the PKT region (Hiesinger et al., 2003; Kato et al.,  
839 2017; Morota et al., 2011). However, the  $\text{TiO}_2$  variation between the LGA magma and young  
840 maria lies within 1 wt.% and is much less than that of the PKT region. This indicates that such a  
841 titanium-rich plume neither provides the young magma directly nor contaminates the magma  
842 source heavily in this farside region. Such a titanium-poor plume in the farside reflects the lunar  
843 dichotomy of IBC distribution. As seen in the  $\text{Mg\#}$  ( $\text{Mg}/(\text{Mg}+\text{Fe})$  in mole per cent) distribution  
844 (Ohtake et al., 2012), the farside crust crystallized from less-evolved magma and could lie over  
845 less IBC than the nearside crust. In addition, several numerical models have predicted that  
846 convection during the mantle overturn makes IBC material in the farside mantle less than that in  
847 the nearside mantle (Parmentier et al., 2002; Zhang et al., 2022).

848

## 849 **7 Conclusions**

850 To estimate the composition of magmatism during lunar ancient expansion, we  
851 investigated spectral and gravity datasets around three craters located on LGAs: Rowland crater  
852 on LGA1, Roche crater on LGA2, and Edison crater on LGA20. Although LGAs have no  
853 prominent spectral feature right above them, LGAs reduced inside these craters suggest that  
854 ancient magma could have been excavated and distributed around them. We first analyzed  
855 spectral absorption with the MI data from Kaguya and  $\text{M}^3$  data from Chandrayaan-1 to  
856 characterize the ejecta from subsurface intrusion. Using an RGB-composite map with the  
857 absorption depth at 950, 1050, and 1250 nm, we surveyed non-mare basaltic exposures. The type  
858 of pyroxene at the discovered exposures is then examined with the MGM spectral deconvolution  
859 method. We next compared the gravity data with gravity simulated with iSALE to discuss  
860 whether the discovered exposures originate from the LGA intrusion or not. After the preparation  
861 of intrusion shape sets by fitting the gravity profile outside the crater, we numerically traced the  
862 subsurface modification, excavation, and porosity change to simulate how the pre-existing LGA  
863 is reduced by the impact.

864 In the case of Rowland, both the spectral and gravity analysis revealed that the LGA  
865 intrusion was not excavated by the cratering. No exposures with a clear indication of high-  
866 calcium pyroxene have been identified around Rowland crater. The simulated gravity does not  
867 match the observed gravity because the gravity signature of intrusion cannot be destroyed due to  
868 the remaining root of the LGA intrusion even after the impact. Thus, the abrupt termination of  
869 LGA at the rim of Rowland cannot be attributed to Rowland's excavation. Considering the low  
870 formation probability of a crater in contact with the LGA terminator, it is the most plausible that  
871 LGA1 formation postdates the Rowland-forming impact, indicating the lunar expansion stage  
872 lasting even after the Nectarian age.

873 In contrast, both Roche and Edison craters enable us to estimate the magma composition  
874 during the lunar expansion. In their peripheries, basaltic exposures are totally found at more than  
875 40 candidates, mostly accompanied by high-calcium pyroxene. Because the possibility of  
876 exogenic contamination, such as ejecta from the mare region, is ruled out, these exposures are  
877 hypothesized to originate from the subsurface LGA intrusion. The gravity simulation with  
878 iSALE also supports this hypothesis. Although Edison crater is too small to quantify the  
879 comparison, a gravity drop similar to LGA2 inside Roche is reproduced in our modeling. In  
880 addition, some exposures are inside the ejecta blanket containing the LGA2 material. After  
881 correcting contamination by highland regolith using the FeO contents, the LGA intrusion is  
882 revealed to be composed of low-titanium magma. In particular, small young maria around LGA2  
883 with ages of 2–3 Ga also consists of low-titanium basalt. This similarity implies that the magma  
884 source region is compositionally uniform over a long period and not contaminated by a plume  
885 from the IBC layer, perhaps reflecting the dichotomy of titanium content inside the lunar mantle.

886

## 887 **Acknowledgments**

888 This work was supported by the IGPEES WINGS Program of the University of Tokyo,  
889 JSPS KAKENHI Grant Number JP22J12387, and JSPS Overseas Challenge Program for Young  
890 Researchers. We gratefully acknowledge the developers of iSALE-2D ([https://isale-  
891 code.github.io](https://isale-code.github.io)), including Kai Wünnemann, Dirk Elbeshausen, Boris Ivanov, and Jay Melosh.  
892 We used pySALEplot to analyze the output file of iSALE and thank Tom Davison for the  
893 development of pySALEPlot. We are also grateful to Hauke Hussmann, Alexander Stark, Mark  
894 Wieczorek, Takahiro Hiroi, and Kosuke Kurosawa for fruitful discussions and helpful  
895 comments. Numerical computations were carried out on the general-purpose PC cluster at the  
896 Center for Computational Astrophysics, National Astronomical Observatory of Japan. Numerical

897 analyses were carried out on the analysis servers at the Center for Computational Astrophysics,  
898 National Astronomical Observatory of Japan.

899

## 900 **Open Research**

901 All the MI datasets can be downloaded via the SELENE data archive system in the Data  
902 ARchives and Transmission System (DARTS) of JAXA

903 (<https://darts.isas.jaxa.jp/planet/pdap/selene/>). The M3 datasets are stored in the PDS Imaging  
904 Node (<https://pds-imaging.jpl.nasa.gov/data/m3/>). All the topography and gravity data

905 (SLDEM2015 and GRGM1200A\_BOUGUER) can be downloaded via the PDS Geoscience

906 Node (<https://pds-geosciences.wustl.edu>). At present, the iSALE shock physics hydrocode is not

907 fully open source, but an application for the use of iSALE may be made through <https://isale->

908 [code.github.io](https://isale-code.github.io).

909

## 910 **References**

- 911 Amsden, A. A., Ruppel, H. M., & Hirt, C. W. (1980). SALE: A Simplified ALE computer program for fluid flow at  
912 all speeds. *Los Alamos National Laboratories Report, LA-8095*(June), 101p. Retrieved from  
913 [http://www.iaea.org/inis/collection/NCLCollectionStore/\\_Public/11/571/11571883.pdf?origin=publication\\_](http://www.iaea.org/inis/collection/NCLCollectionStore/_Public/11/571/11571883.pdf?origin=publication_detail)  
914 [ail](http://www.iaea.org/inis/collection/NCLCollectionStore/_Public/11/571/11571883.pdf?origin=publication_detail)
- 915 Andrews-Hanna, J. C., Asmar, S. W., Head, J. W., Kiefer, W. S., Konopliv, A. S., Lemoine, F. G., et al. (2013).  
916 Ancient igneous intrusions and early expansion of the moon revealed by GRAIL gravity gradiometry. *Science*,  
917 *339*(6120), 675–678. <https://doi.org/10.1126/science.1231753>
- 918 Andrews-Hanna, J. C., Head, J. W., Johnson, B. C., Keane, J. T., Kiefer, W. S., McGovern, P. J., et al. (2018). Ring  
919 faults and ring dikes around the Orientale basin on the Moon. *Icarus*, *310*, 1–20.  
920 <https://doi.org/10.1016/j.icarus.2017.12.012>
- 921 Barker, M. K., Mazarico, E., Neumann, G. A., Zuber, M. T., Haruyama, J., & Smith, D. E. (2016). A new lunar  
922 digital elevation model from the Lunar Orbiter Laser Altimeter and SELENE Terrain Camera. *Icarus*, *273*,  
923 346–355. <https://doi.org/10.1016/j.icarus.2015.07.039>
- 924 Besse, S., Sunshine, J., Staid, M., Boardman, J., Pieters, C., Guasqui, P., et al. (2013). A visible and near-infrared  
925 photometric correction for Moon Mineralogy Mapper (M3). *Icarus*, *222*(1), 229–242.  
926 <https://doi.org/10.1016/j.icarus.2012.10.036>
- 927 Besse, S., Sunshine, J. M., & Gaddis, L. R. (2014). Volcanic glass signatures in spectroscopic survey of newly  
928 proposed lunar pyroclastic deposits. *Journal of Geophysical Research: Planets*, *119*(2), 355–372.  
929 <https://doi.org/10.1002/2013JE004537>
- 930 Boardman, J. W., Pieters, C. M., Green, R. O., Lundeen, S. R., Varanasi, P., Nettles, J., et al. (2011). Measuring  
931 moonlight: An overview of the spatial properties, lunar coverage, selenolocation, and related Level 1B

- 932 products of the Moon Mineralogy Mapper. *Journal of Geophysical Research: Planets*, 116(6), 1–15.  
 933 <https://doi.org/10.1029/2010JE003730>
- 934 Bottke, W. F., Vokrouhlický, D., Minton, D., Nesvorný, D., Morbidelli, A., Brasser, R., et al. (2012). An Archaean  
 935 heavy bombardment from a destabilized extension of the asteroid belt. *Nature*, 485(7396), 78–81.  
 936 <https://doi.org/10.1038/nature10967>
- 937 Clark, R. N., Pieters, C. M., Green, R. O., Boardman, J. W., & Petro, N. E. (2011). Thermal removal from near-  
 938 infrared imaging spectroscopy data of the Moon. *Journal of Geophysical Research: Planets*, 116(6), 1–9.  
 939 <https://doi.org/10.1029/2010JE003751>
- 940 Cloutis, E. A., & Gaffey, M. J. (1991). Pyroxene spectroscopy revisited: spectral-compositional correlations and  
 941 relationship to geothermometry. *Journal of Geophysical Research*, 96(E5). <https://doi.org/10.1029/91je02512>
- 942 Collins, G. S. (2014). Numerical simulations of impact crater formation with dilatancy. *Journal of Geophysical  
 943 Research: Planets*, 119(12), 2600–2619. <https://doi.org/10.1002/2014JE004708>
- 944 Collins, G. S., Melosh, H. J., & Wünnemann, K. (2011). Improvements to the  $\epsilon$ - $\alpha$  Porous compaction model for  
 945 simulating impacts into high-porosity solar system objects. *International Journal of Impact Engineering*,  
 946 38(6), 434–439. <https://doi.org/10.1016/j.ijimpeng.2010.10.013>
- 947 Collins, Gareth S., Melosh, H. J., & Ivanov, B. A. (2004). Modeling damage and deformation in impact simulations.  
 948 *Meteoritics and Planetary Science*, 39(2), 217–231. <https://doi.org/10.1111/j.1945-5100.2004.tb00337.x>
- 949 Corley, L. M., McGovern, P. J., Kramer, G. Y., Lemelin, M., Trang, D., Gillis-Davis, J. J., et al. (2018). Olivine-  
 950 bearing lithologies on the Moon: Constraints on origins and transport mechanisms from M3 spectroscopy,  
 951 radiative transfer modeling, and GRAIL crustal thickness. *Icarus*, 300, 287–304.  
 952 <https://doi.org/10.1016/j.icarus.2017.09.012>
- 953 Davison, T. M., & Collins, G. S. (2022). Complex Crater Formation by Oblique Impacts on the Earth and Moon.  
 954 *Geophysical Research Letters*, 49(21), 1–9. <https://doi.org/10.1029/2022gl101117>
- 955 Delano, J. W. (1990). Buoyancy-driven melt segregation in the Earth's Moon. I. Numerical results. In *Lunar and  
 956 Planetary Science Conference, 20th, Houston, TX, Mar. 13-17, 1989, Proceedings (A90-33456 14-91).  
 957 Houston, TX, Lunar and Planetary Institute, 1990, p. 3-12. (Vol. 4, pp. 3–12).*
- 958 Denevi, B. W., Lucey, P. G., Hochberg, E. J., & Steutel, D. (2007). Near-infrared optical constants of pyroxene as a  
 959 function of iron and calcium content. *Journal of Geophysical Research*, 112(E5), E05009.  
 960 <https://doi.org/10.1029/2006JE002802>
- 961 Elkins-Tanton, L. T., Burgess, S., & Yin, Q. Z. (2011). The lunar magma ocean: Reconciling the solidification  
 962 process with lunar petrology and geochronology. *Earth and Planetary Science Letters*, 304(3–4), 326–336.  
 963 <https://doi.org/10.1016/j.epsl.2011.02.004>
- 964 Giguere, T. A., Hawke, B. R., Blewett, D. T., Bussey, D. B. J., Lucey, P. G., Smith, G. A., et al. (2003). Remote  
 965 sensing studies of the Lomonosov-Fleming region of the Moon. *Journal of Geophysical Research: Planets*,  
 966 108(11). <https://doi.org/10.1029/2003je002069>
- 967 Green, R. O., Pieters, C., Mouroulis, P., Eastwood, M., Boardman, J., Glavich, T., et al. (2011). The Moon  
 968 Mineralogy Mapper (M3) imaging spectrometer for lunar science: Instrument description, calibration, on-orbit  
 969 measurements, science data calibration and on-orbit validation. *Journal of Geophysical Research: Planets*,  
 970 116(10), 1–31. <https://doi.org/10.1029/2011JE003797>
- 971 Head, J. W., & Wilson, L. (2017). Generation, ascent and eruption of magma on the Moon: New insights into source  
 972 depths, magma supply, intrusions and effusive/explosive eruptions (Part 2: Predicted emplacement processes  
 973 and observations). *Icarus*, 283, 176–223. <https://doi.org/10.1016/j.icarus.2016.05.031>
- 974 Head, J. W., Fassett, C. I., Kadish, S. J., Smith, D. E., Zuber, M. T., Neumann, G. A., & Mazarico, E. (2010). Global  
 975 distribution of large lunar craters: Implications for resurfacing and impactor populations. *Science*, 329(5998),  
 976 1504–1507. <https://doi.org/10.1126/science.1195050>
- 977 Hess, P. C., & Parmentier, E. M. (1995). A model for the thermal and chemical evolution of the Moon's interior:  
 978 implications for the onset of mare volcanism. *Earth and Planetary Science Letters*, 134(3–4), 501–514.  
 979 [https://doi.org/10.1016/0012-821X\(95\)00138-3](https://doi.org/10.1016/0012-821X(95)00138-3)
- 980 Heyer, T., Iqbal, W., Oetting, A., Hiesinger, H., van der Bogert, C. H., & Schmedemann, N. (2023). A comparative  
 981 analysis of global lunar crater catalogs using OpenCraterTool – An open source tool to determine and compare  
 982 crater size-frequency measurements. *Planetary and Space Science*, 231(January), 105687.  
 983 <https://doi.org/10.1016/j.pss.2023.105687>
- 984 Hiesinger, H., Head, J. W., Wolf, U., Jaumann, R., & Neukum, G. (2003). Ages and stratigraphy of mare basalts in  
 985 Oceanus Procellarum, Mare Nubium, mare Cognitum, and Mare Insularum. *Journal of Geophysical Research:  
 986 Planets*, 108(7). <https://doi.org/10.1029/2002je001985>

- 987 Hiesinger, H., van der Bogert, C. H., Thiessen, F., & Robinson, M. S. (2013). Absolute Model Ages of Light Plains  
988 in the Southern Lunar Hemisphere. *Lunar and Planetary Science Conference*, 4–5.
- 989 Isaacson, P. J., Pieters, C. M., Besse, S., Clark, R. N., Head, J. W., Klima, R. L., et al. (2011). Remote compositional  
990 analysis of lunar olivine-rich lithologies with Moon Mineralogy Mapper (M3) spectra. *Journal of Geophysical  
991 Research: Planets*, 116(4), 1–17. <https://doi.org/10.1029/2010JE003731>
- 992 Isaacson, P. J., Petro, N. E., Pieters, C. M., Besse, S., Boardman, J. W., Clark, R. N., et al. (2013). Development,  
993 importance, and effect of a ground truth correction for the Moon Mineralogy Mapper reflectance data set.  
994 *Journal of Geophysical Research: Planets*, 118(3), 369–381. <https://doi.org/10.1002/jgre.20048>
- 995 Ivanov, B. A., Deniém, D., & Neukum, G. (1997). Implementation of dynamic strength models into 2D hydrocodes:  
996 Applications for atmospheric breakup and impact cratering. *International Journal of Impact Engineering*,  
997 20(1–5), 411–430. [https://doi.org/10.1016/s0734-743x\(97\)87511-2](https://doi.org/10.1016/s0734-743x(97)87511-2)
- 998 Kato, S., Morota, T., Yamaguchi, Y., Watanabe, S. I., Otake, H., & Ohtake, M. (2017). Magma source transition of  
999 lunar mare volcanism at 2.3 Ga. *Meteoritics and Planetary Science*, 52(9), 1899–1915.  
1000 <https://doi.org/10.1111/maps.12896>
- 1001 Kiefer, W. S., MacKe, R. J., Britt, D. T., Irving, A. J., & Consolmagno, G. J. (2012). The density and porosity of  
1002 lunar rocks. *Geophysical Research Letters*, 39(7). <https://doi.org/10.1029/2012GL051319>
- 1003 Klima, R. L., Pieters, C. M., & Dyar, M. D. (2007). Spectroscopy of synthetic Mg-Fe pyroxenes I: Spin-allowed and  
1004 spin-forbidden crystal field bands in the visible and near-infrared. *Meteoritics and Planetary Science*, 42(2),  
1005 235–253. <https://doi.org/10.1111/j.1945-5100.2007.tb00230.x>
- 1006 Klima, R. L., Dyar, M. D., & Pieters, C. M. (2011). Near-infrared spectra of clinopyroxenes: Effects of calcium  
1007 content and crystal structure. *Meteoritics and Planetary Science*, 46(3), 379–395.  
1008 <https://doi.org/10.1111/j.1945-5100.2010.01158.x>
- 1009 Krüger, T., van der Bogert, C. H., & Hiesinger, H. (2016). Geomorphologic mapping of the lunar crater Tycho and  
1010 its impact melt deposits. *Icarus*, 273, 164–181. <https://doi.org/10.1016/j.icarus.2016.02.018>
- 1011 Kumaresan, P. R., & Saravanavel, J. (2022). Compositional Mapping and Spectral Analysis of Sulpicius Gallus  
1012 Dark Mantling Deposits Using Lunar Orbital Data Sets Including Chandrayaan-1 Moon Mineralogy Mapper.  
1013 *Journal of the Indian Society of Remote Sensing*, 50(7), 1301–1319. <https://doi.org/10.1007/s12524-022-01529-4>
- 1014
- 1015 Laneuville, M., Wiczorek, M. A., Breuer, D., & Tosi, N. (2013). Asymmetric thermal evolution of the Moon.  
1016 *Journal of Geophysical Research: Planets*, 118(7), 1435–1452. <https://doi.org/10.1002/jgre.20103>
- 1017 Lemoine, F. G., Goossens, S., Sabaka, T. J., Nicholas, J. B., Mazarico, E., Rowlands, D. D., et al. (2014).  
1018 GRGM900C: A degree 900 lunar gravity model from GRAIL primary and extended mission data.  
1019 *Geophysical Research Letters*, 41(10), 3382–3389. <https://doi.org/10.1002/2014GL060027>
- 1020 Li, Q. L., Zhou, Q., Liu, Y., Xiao, Z., Lin, Y., Li, J. H., et al. (2021). Two-billion-year-old volcanism on the Moon  
1021 from Chang'e-5 basalts. *Nature*, 600(7887), 54–58. <https://doi.org/10.1038/s41586-021-04100-2>
- 1022 Liang, W., & Andrews-Hanna, J. C. (2022). Probing the source of ancient linear gravity anomalies on the Moon.  
1023 *Icarus*, 380. <https://doi.org/10.1016/j.icarus.2022.114978>
- 1024 Liu, T., Luther, R., Manske, L., & Wünnemann, K. (2022). Melt Production and Ejection From Lunar Intermediate-  
1025 Sized Impact Craters: Where Is the Molten Material Deposited? *Journal of Geophysical Research: Planets*,  
1026 127(8), 1–13. <https://doi.org/10.1029/2022JE007264>
- 1027 Lucey, P. G., Taylor, G. J., Hawke, B. R., & Spudis, P. D. (1998). FeO and TiO<sub>2</sub> concentrations in the South Pole-  
1028 Aitken basin: Implications for mantle composition and basin formation. *Journal of Geophysical Research:*  
1029 *Planets*, 103(E2), 3701–3708. <https://doi.org/10.1029/97JE03146>
- 1030 Lucey, P. G., Blewett, D. T., Taylor, G. J., & Hawke, B. R. (2000). Imaging of lunar surface maturity. *Journal of*  
1031 *Geophysical Research: Planets*, 105(E8), 20377–20386. <https://doi.org/10.1029/1999JE001110>
- 1032 Lucey, P. G., Blewett, D. T., & Jolliff, B. L. (2000). Lunar iron and titanium abundance algorithms based on final  
1033 processing of Clementine ultraviolet-visible images. *Journal of Geophysical Research: Planets*, 105(E8),  
1034 20297–20305. <https://doi.org/10.1029/1999JE001117>
- 1035 Lucey, P. G., Norman, J. A., Crites, S. T., Taylor, G. J., Hawke, B. R., Lemelin, M., & Melosh, H. J. (2014). A large  
1036 spectral survey of small lunar craters: Implications for the composition of the lunar mantle. *American*  
1037 *Mineralogist*, 99(11–12), 2251–2257. <https://doi.org/10.2138/am-2014-4854>
- 1038 McGetchin, T. R., Settle, M., & Head, J. W. (1973). Radial Thickness Variation in Impact Crater Ejecta :, 20, 226–  
1039 236.
- 1040 Melosh, H. J. (1989). *Impact cratering : a geologic process*. New York ; Oxford: Oxford University Press ;  
1041 Clarendon Press. Retrieved from <http://www.loc.gov/catdir/enhancements/fy0638/88005353-t.html>

- 1042 Melosh, H. J., Ryan, E. V., & Asphaug, E. (1992). Dynamic fragmentation in impacts: Hydrocode simulation of  
 1043 laboratory impacts. *Journal of Geophysical Research*, 97(E9), 14735. <https://doi.org/10.1029/92JE01632>
- 1044 Melosh, H. J., Freed, A. M., Johnson, B. C., Blair, D. M., Andrews-Hanna, J. C., Neumann, G. A., et al. (2013). The  
 1045 origin of lunar mascon basins. *Science*, 340(6140), 1552–1555. <https://doi.org/10.1126/science.1235768>
- 1046 Michaut, C., Pinel, V., & Maccaferri, F. (2020). Magma ascent at floor-fractured craters diagnoses the lithospheric  
 1047 stress state on the Moon. *Earth and Planetary Science Letters*, 530, 115889.  
 1048 <https://doi.org/10.1016/j.epsl.2019.115889>
- 1049 Milbury, C., Johnson, B. C., Melosh, H. J., Collins, G. S., Blair, D. M., Soderblom, J. M., et al. (2015). Preimpact  
 1050 porosity controls the gravity signature of lunar craters. *Geophysical Research Letters*, 42(22), 9711–9716.  
 1051 <https://doi.org/10.1002/2015GL066198>
- 1052 Miljković, K., Wieczorek, M. A., Laneuville, M., Nemchin, A., Bland, P. A., & Zuber, M. T. (2021). Large impact  
 1053 cratering during lunar magma ocean solidification. *Nature Communications*, 12(1), 1–18.  
 1054 <https://doi.org/10.1038/s41467-021-25818-7>
- 1055 Miljković, Katarina, Wieczorek, M. A., Collins, G. S., Solomon, S. C., Smith, D. E., & Zuber, M. T. (2015).  
 1056 Excavation of the lunar mantle by basin-forming events on the Moon. *Earth and Planetary Science Letters*,  
 1057 409, 243–251. <https://doi.org/10.1016/j.epsl.2014.10.041>
- 1058 Moore, H. J., Hodges, C. A., & Scott, D. H. (1974). Multiringed basins - Illustrated by Orientale and associated  
 1059 features. *Proc. Lunar Sci. Conf. 5th., 1*, 71–100.
- 1060 Moriarty, D. P., & Pieters, C. M. (2018). The Character of South Pole-Aitken Basin: Patterns of Surface and  
 1061 Subsurface Composition. *Journal of Geophysical Research: Planets*, 123(3), 729–747.  
 1062 <https://doi.org/10.1002/2017JE005364>
- 1063 Morota, T., Haruyama, J., Ohtake, M., Matsunaga, T., Honda, C., Yokota, Y., et al. (2011). Timing and  
 1064 characteristics of the latest mare eruption on the Moon. *Earth and Planetary Science Letters*, 302(3–4), 255–  
 1065 266. <https://doi.org/10.1016/j.epsl.2010.12.028>
- 1066 Neal, C. R., & Taylor, L. A. (1992). Petrogenesis of mare basalts: A record of lunar volcanism. *Geochimica et*  
 1067 *Cosmochimica Acta*, 56(6), 2177–2211. [https://doi.org/10.1016/0016-7037\(92\)90184-K](https://doi.org/10.1016/0016-7037(92)90184-K)
- 1068 Ogawa, Y., Matsunaga, T., Nakamura, R., Saiki, K., Ohtake, M., Hiroi, T., et al. (2011). The widespread occurrence  
 1069 of high-calcium pyroxene in bright-ray craters on the Moon and implications for lunar-crust composition.  
 1070 *Geophysical Research Letters*, 38(17). <https://doi.org/10.1029/2011GL048569>
- 1071 Ohtake, M., Haruyama, J., Matsunaga, T., Kodama, S., Morota, T., & Yokota, Y. (2008). Scientific objectives and  
 1072 specification of the SELENE Multiband Imager. *Advances in Space Research*, 42(2), 301–304.  
 1073 <https://doi.org/10.1016/j.asr.2007.04.041>
- 1074 Ohtake, M., Pieters, C. M., Isaacson, P., Besse, S., Yokota, Y., Matsunaga, T., et al. (2013). One Moon, Many  
 1075 Measurements 3: Spectral reflectance. *Icarus*, 226(1), 364–374. <https://doi.org/10.1016/j.icarus.2013.05.010>
- 1076 Ohtake, M., Uemoto, K., Yokota, Y., Morota, T., Yamamoto, S., Nakamura, R., et al. (2014). Geologic structure  
 1077 generated by large-impact basin formation observed at the South Pole-Aitken basin on the Moon. *Geophysical*  
 1078 *Research Letters*, 41(8), 2738–2745. <https://doi.org/10.1002/2014GL059478>
- 1079 Ohtake, Makiko, Takeda, H., Matsunaga, T., Yokota, Y., Haruyama, J., Morota, T., et al. (2012). Asymmetric  
 1080 crustal growth on the Moon indicated by primitive farside highland materials. *Nature Geoscience*, 5(6), 384–  
 1081 388. <https://doi.org/10.1038/ngeo1458>
- 1082 Otake, H., Ohtake, M., & Hirata, N. (2012). Lunar Iron and Titanium Abundance Algorithms Based on SELENE  
 1083 (Kaguya) Multiband Imager Data (p. 1905). Texas: 43rd Lunar and Planetary Science Conference.
- 1084 Parmentier, E. M., Zhong, S., & Zuber, M. T. (2002). Gravitational differentiation due to initial chemical  
 1085 stratification: origin of lunar asymmetry by the creep of dense KREEP? *Earth and Planetary Science Letters*,  
 1086 201(3–4), 473–480. [https://doi.org/10.1016/S0012-821X\(02\)00726-4](https://doi.org/10.1016/S0012-821X(02)00726-4)
- 1087 Pasckert, J. H., Hiesinger, H., & van der Bogert, C. H. (2015a). Small-scale lunar farside volcanism. *Icarus*, 257,  
 1088 336–354. <https://doi.org/10.1016/j.icarus.2015.04.040>
- 1089 Pasckert, J. H., Hiesinger, H., & van der Bogert, C. H. (2015b). Small-scale lunar farside volcanism. *Icarus*, 257,  
 1090 336–354. <https://doi.org/10.1016/j.icarus.2015.04.040>
- 1091 Pieters, C. M., Goswami, J. N., Clark, R. N., Annadurai, M., Boardman, J., Buratti, B., et al. (2009). Character and  
 1092 spatial distribution of OH/H<sub>2</sub>O on the surface of the moon seen by M3 on chandrayaan-1. *Science*, 326(5952),  
 1093 568–572. <https://doi.org/10.1126/science.1178658>
- 1094 Piskorz, D., & Stevenson, D. J. (2014). The formation of pure anorthosite on the Moon. *Icarus*, 239, 238–243.  
 1095 <https://doi.org/10.1016/j.icarus.2014.06.015>

- 1096 Sato, H., Robinson, M. S., Lawrence, S. J., Denevi, B. W., Hapke, B., Jolliff, B. L., & Hiesinger, H. (2017). Lunar  
1097 mare TiO<sub>2</sub> abundances estimated from UV/Vis reflectance. *Icarus*, *296*, 216–238.  
1098 <https://doi.org/10.1016/j.icarus.2017.06.013>
- 1099 Sawada, N., Morota, T., Kato, S., Ishihara, Y., & Hiramatsu, Y. (2016). Constraints on timing and magnitude of  
1100 early global expansion of the Moon from topographic features in linear gravity anomaly areas. *Geophysical*  
1101 *Research Letters*, *43*(10), 4865–4870. <https://doi.org/10.1002/2016GL068966>
- 1102 Shuvalov, V. (2011). Ejecta deposition after oblique impacts: An influence of impact scale. *Meteoritics and*  
1103 *Planetary Science*, *46*(11), 1713–1718. <https://doi.org/10.1111/j.1945-5100.2011.01259.x>
- 1104 Snyder, G. A., Taylor, L. A., & Neal, C. R. (1992). A chemical model for generating the sources of mare basalts:  
1105 Combined equilibrium and fractional crystallization of the lunar magmasphere. *Geochimica et Cosmochimica*  
1106 *Acta*, *56*(10), 3809–3823. [https://doi.org/10.1016/0016-7037\(92\)90172-F](https://doi.org/10.1016/0016-7037(92)90172-F)
- 1107 Soderblom, J. M., Evans, A. J., Johnson, B. C., Melosh, H. J., Miljkovic, K., Phillips, R. J., et al. (2015). The  
1108 fractured Moon: Production and saturation of porosity in the lunar highlands from impact cratering.  
1109 *Geophysical Research Letters*, *42*(17), 6939–6944. <https://doi.org/10.1002/2015GL065022>
- 1110 Sunshine, J. M., Pieters, C. M., & Pratt, S. F. (1990). Deconvolution of mineral absorption bands: an improved  
1111 approach. *Journal of Geophysical Research*, *95*(B5), 6955–6966. <https://doi.org/10.1029/JB095iB05p06955>
- 1112 Taguchi, M., Morota, T., & Kato, S. (2017). Lateral heterogeneity of lunar volcanic activity according to volumes of  
1113 mare basalts in the farside basins. *Journal of Geophysical Research: Planets*, *122*(7), 1505–1521.  
1114 <https://doi.org/10.1002/2016JE005246>
- 1115 Tian, H. C., Wang, H., Chen, Y., Yang, W., Zhou, Q., Zhang, C., et al. (2021). Non-KREEP origin for Chang’e-5  
1116 basalts in the Procellarum KREEP Terrane. *Nature*, *600*(7887), 59–63. [https://doi.org/10.1038/s41586-021-](https://doi.org/10.1038/s41586-021-04119-5)  
1117 [04119-5](https://doi.org/10.1038/s41586-021-04119-5)
- 1118 U, K., Hasumi, H., & Ogawa, M. (2022). Effects of magma-generation and migration on the expansion and  
1119 contraction history of the Moon. *Earth, Planets and Space*, *74*(1). <https://doi.org/10.1186/s40623-022-01631-4>
- 1120 de Vries, J., van den Berg, A., & van Westrenen, W. (2010). Formation and evolution of a lunar core from ilmenite-  
1121 rich magma ocean cumulates. *Earth and Planetary Science Letters*, *292*(1–2), 139–147.  
1122 <https://doi.org/10.1016/j.epsl.2010.01.029>
- 1123 Wang, Y., Wu, B., Xue, H., Li, X., & Ma, J. (2021). An Improved Global Catalog of Lunar Impact Craters ( $\geq 1$  km)  
1124 With 3D Morphometric Information and Updates on Global Crater Analysis. *Journal of Geophysical*  
1125 *Research: Planets*, *126*(9), 1–25. <https://doi.org/10.1029/2020JE006728>
- 1126 Watanabe, T., Masuyama, T., Nagaoka, K., & Tahara, T. (2002). Analog experiments on magma-filled cracks:  
1127 Competition between external stresses and internal pressure. *Earth, Planets and Space*, *54*(12), 1247–1261.  
1128 <https://doi.org/10.1186/bf03352453>
- 1129 Whitten, J., & Head, J. (2015a). Lunar cryptomaria: Physical characteristics, distribution, and implications for  
1130 ancient volcanism. *Icarus*, *247*, 150–171. <https://doi.org/10.1016/j.icarus.2014.09.031>
- 1131 Whitten, J., & Head, J. W. (2015b). Lunar cryptomaria: Mineralogy and composition of ancient volcanic deposits.  
1132 *Planetary and Space Science*, *106*, 67–81. <https://doi.org/10.1016/j.pss.2014.11.027>
- 1133 Wilhelms, D. E., & El-Baz, F. (1977). *Geologic map of the east side of the Moon*. IMAP.  
1134 <https://doi.org/10.3133/i948>
- 1135 Wilson, L., & Head, J. W. (2017). Generation, ascent and eruption of magma on the Moon: New insights into source  
1136 depths, magma supply, intrusions and effusive/explosive eruptions (Part 1: Theory). *Icarus*, *283*, 146–175.  
1137 <https://doi.org/10.1016/j.icarus.2015.12.039>
- 1138 Wünnemann, K., Collins, G. S., & Melosh, H. J. (2006). A strain-based porosity model for use in hydrocode  
1139 simulations of impacts and implications for transient crater growth in porous targets. *Icarus*, *180*(2), 514–527.  
1140 <https://doi.org/10.1016/j.icarus.2005.10.013>
- 1141 Yamamoto, S., & Watanabe, S. (2021). Characterization of D-Type Spectra Based on Hyperspectral Remote  
1142 Sensing of the Lunar Surface. *Journal of Geophysical Research: Planets*, *126*(1).  
1143 <https://doi.org/10.1029/2020JE006669>
- 1144 Yamamoto, S., Nakamura, R., Matsunaga, T., Ogawa, Y., Ishihara, Y., Morota, T., et al. (2015). Global occurrence  
1145 trend of high-Ca pyroxene on lunar highlands and its implications. *Journal of Geophysical Research: Planets*,  
1146 *120*(5), 831–848. <https://doi.org/10.1002/2014JE004740>
- 1147 Yamamoto, S., Watanabe, S., & Matsunaga, T. (2018). Space-Weathered Anorthosite as Spectral D-Type Material  
1148 on the Martian Satellites. *Geophysical Research Letters*, *45*(3), 1305–1312.  
1149 <https://doi.org/10.1002/2017GL076612>

- 1150 Yokota, Y., Matsunaga, T., Ohtake, M., Haruyama, J., Nakamura, R., Yamamoto, S., et al. (2011). Lunar  
1151 photometric properties at wavelengths 0.5-1.6 $\mu$ m acquired by SELENE Spectral Profiler and their dependency  
1152 on local albedo and latitudinal zones. *Icarus*, 215(2), 639–660. <https://doi.org/10.1016/j.icarus.2011.07.028>  
1153 Zhang, D., Su, B., Chen, Y., Yang, W., Mao, Q., & Jia, L. H. (2022, April 1). Titanium in olivine reveals low-Ti  
1154 origin of the Chang'E-5 lunar basalts. *Lithos*. Elsevier B.V. <https://doi.org/10.1016/j.lithos.2022.106639>  
1155 Zhang, N., Parmentier, E. M., & Liang, Y. (2013a). A 3-D numerical study of the thermal evolution of the Moon  
1156 after cumulate mantle overturn: The importance of rheology and core solidification. *Journal of Geophysical*  
1157 *Research: Planets*, 118(9), 1789–1804. <https://doi.org/10.1002/jgre.20121>  
1158 Zhang, N., Parmentier, E. M., & Liang, Y. (2013b). Effects of lunar cumulate mantle overturn and megaregolith on  
1159 the expansion and contraction history of the Moon. *Geophysical Research Letters*, 40(19), 5019–5023.  
1160 <https://doi.org/10.1002/grl.50988>  
1161 Zhang, Nan, Ding, M., Zhu, M. H., Li, H., Li, H., & Yue, Z. (2022). Lunar compositional asymmetry explained by  
1162 mantle overturn following the South Pole–Aitken impact. *Nature Geoscience*, 15(1), 37–41.  
1163 <https://doi.org/10.1038/s41561-021-00872-4>  
1164 Zhao, Y., de Vries, J., van den Berg, A. P., Jacobs, M. H. G., & van Westrenen, W. (2019). The participation of  
1165 ilmenite-bearing cumulates in lunar mantle overturn. *Earth and Planetary Science Letters*, 511, 1–11.  
1166 <https://doi.org/10.1016/j.epsl.2019.01.022>  
1167 Zuber, M. T., Smith, D. E., Watkins, M. M., Asmar, S. W., Konopliv, A. S., Lemoine, F. G., et al. (2013). Gravity  
1168 field of the moon from the Gravity Recovery and Interior Laboratory (GRAIL) mission. *Science*, 339(6120),  
1169 668–671. <https://doi.org/10.1126/science.1231507>  
1170